ELSEVIER

Journal of Hazardous Materials 56 (1997) 59–105

JOURNAL OF HAZARDOUS MATERIALS

Field experiments with dispersion of pressure liquefied ammonia

Morten Nielsen [a,*], Søren Ott [a], Hans E. Jørgensen [a], Roland Bengtsson [b], Kenneth Nyrén [c,1], Stellan Winter [c], David Ride [d,2], Chris Jones [d]

[a] *Risø National Laboratory, Meteorology and Wind Energy Department, P.O. Box 49, DK-4000 Roskilde, Denmark*

[b] *Hydro-Care Safety Academy, P.O. Box 516, S-26124 Landskrona, Sweden*

[c] *FOA, Cementvägen 20, S-90182 Umeå, Sweden*

[d] *CBDE, P.O. Box 37, Salisbury SP4 0JQ, UK*

Received 16 June 1996; accepted 10 February 1997

Abstract

This paper presents dispersion experiments with continuous releases of liquefied ammonia carried out during the CEC ENVIRONMENT project "Fladis Field Experiments". The source was a horizontal flash boiling jet with release rates of 0.25–0.5 kg s^{-1}. The objective was to study the dispersion in all its stages at the source, in the heavy jet with aerosols, the slightly stabilized plume, and further downstream into the regime of passive dispersion. The concentration field is analyzed in a fixed frame of reference as well as a frame of reference moving with the instantaneous plume centre-line. Empirical probability functions and a spatial correlation of the concentration fluctuations are found, and the enthalpy balance of the cold heavy jet and the aerosol composition are evaluated. © 1997 Elsevier Science B.V.

Keywords: Aerosols; Ammonia; Concentration; Dispersion; Enthalpy; Field experiments; Fluctuations; Heavy gas; Jet; Meandering; Plume; Source; Statistics

1. Introduction

An accidental release of a pressure liquefied gas often results in a cloud which is heavier than air. Initially the dispersion of such a release is influenced by gravity, but as

* Corresponding author. Fax: +45 4677 4677; E-mail: n.m.nielsen@risoe.dk.

[1] Present affiliation: EriSoft AB, Box 4205, S-90406 Umeå, Sweden.

[2] Present affiliation: 19 Parkland Way, Porton Salisbury, SP4 0LY, UK.

PII S0304-3894(97)00029-0

the gas is diluted with air, the cloud density will gradually approach that of the ambient. If the released substance is sufficiently toxic, the weak concentrations in the regime of passive dispersion will also be hazardous. Accurate prediction of these downstream concentrations requires knowledge of the dispersion process in all its stages from the source through a heavy-gas phase to passive atmospheric dispersion. In practice the risk engineer may have to apply a chain of numerical models, where the output of the first computation is used as input to the next one, etc. This is not an ideal approach since the uncertainty of the calculations accumulates, and it is not obvious exactly where to make the transition from one stage of the dispersion to the next one. Publicly available heavy-gas dispersion models (e.g. HEGADAS [1], DEGADIS [2], SLAM [3], and DRIFT [4]) use similar concepts. The typical heavy plume model has an interface to a source module which is selected according to the release type, and the dispersion code is usually designed with a smooth transition from heavy-gas spreading to a passive Gaussian plume. Webber and Kukkonen [5] found that gravitational spreading and jet momentum were likely to co-exist in a typical two-phase jet release and warned against the idea of transition from an pure jet to a momentumless heavy-gas plume.

The present field experiment project was linked to the project *Research on the Dispersion of Two-phase Flashing Releases* (Fladis) which was part of the STEP Programme of the Commission of the European Communities. A list of project partners is given in the acknowledgment section. The objectives of the main Fladis project were the following, as listed in the final project report by Duijm [6].

- To quantify by numerical modelling the behaviour of the source term of ammonia with special emphasis on aerosol modelling.
- To quantify the near-field heavy-gas dispersion behaviour of ammonia and the far-field passive dispersion by wind-tunnel experiments and by "simple" and three-dimensional (CFD) mathematical modelling.
- To quantify the influence of obstacles and terrain effects on the dispersion in the near- and far-field including concentration fluctuations.

Field data on the interaction between a dense gas plume and simple obstacles were available from a previous series of propane experiments, see Heinrich and Scherwinski [7] and Nielsen and Jensen [8]. New data were needed on the behaviour of a flash boiling ammonia jet and on the transition from dense gas spreading to passive dispersion. The main objective of the Fladis field experiment project was to provide this information.

The Fladis project had two reasons to focus on ammonia releases. First the hazards of ammonia are of interest because of its toxicity and increasing use in industry, e.g. as an alternative cooling agent substituting freon or as a compound used in smoke denitrification units at fossil fuel power plants. Secondly the density of an ammonia cloud is a delicate balance which depends on the air moisture and heat input from the ground as explained by Kaiser and Walker [9]. The molar weight of ammonia is less than that of air, and an ammonia plume can only be heavy because of the temperature deficit caused by initial evaporation. Heat transfer from the surroundings, condensation of the water component of entrained humid air, and possible deposition of liquid aerosols modifies the density difference between the cloud and the ambient. The mathematical modelling of simultaneous two-phase thermodynamics and dispersion dynamics is greatly simpli-

fied by an assumption of homogeneous thermal and vapour pressure equilibrium between aerosols and the surrounding gas phase. Kukkonen et al. [10] compared the state of a binary water/ammonia aerosol ventilated by its fall velocity and evaporating in a moist atmosphere to the simple homogeneous equilibrium approximation. An aerosol is of course not in equilibrium during evaporation, but it was concluded that the homogeneous equilibrium model gave sufficiently accurate results for aerosol diameters less than 100 μm. This condition is met in flash boiling jets from high pressure liquefied gas storages such as in the present experiments, whereas emission from semi-refrigerated storages may result in aerosols large enough to invalidate the homogeneous equilibrium approximation. Webber et al. [11] expressed the phase equilibrium equations in a differential form which linked the rate of temperature and composition change to the rates of air entrainment and aerosol deposition. These formulae were implemented as interchangeable modules for the DRIFT heavy-gas dispersion model applicable for contaminants which either (1) are immiscible with water, (2) form ideal solutions, (3) form hygroscopic solutions (ammonia), or (4) involve gas-phase reactions (hydrogen fluoride), see Webber et al. [4]. Hydrogen fluoride is hygroscopic like ammonia and its use is of great concern because of the associated hazards and difficulties in dispersion modelling, see Lines [12]. The non-isothermal laboratory experiments of Meroney and Neff [13] and Ruff et al. [14] showed that heat transfer from the ground reduced the excess density of cold gas releases. According to the analysis of Britter [15] it is, however, not possible to extrapolate such laboratory results to large scale without violating the scaling laws either for heat transfer or for heavy-gas dispersion.

The most well-known liquefied ammonia dispersion experiments are the Desert Tortoise series, see Goldwire et al. [16]. The release rates in Desert Tortoise were O(100) kg s^{-1}, which is much higher than those in the present experiments, and the dispersion was therefore more affected by gravity. In the Desert Tortoise experiments a pool of liquid ammonia formed in front of the spill point, but because of differences in the release system this never happened in the present experiments. Other differences are the lower ambient temperature and higher air humidity in Fladis, which are more representative for a European climate. Generally the release durations were longer than those in Desert Tortoise. We are aware of two additional heavy-gas experiments with ammonia, i.e. Resplandy [17] and Pfenning et al. [18], but these experiments had a modest instrumentation compared to that of Desert Tortoise and Fladis. Further large-scale ammonia field experiments, focusing on liquid rain-out after jet impingement, are presently (winter 1996/1997) carried out by the Institute National de l'Environment Industriel et des Risques, France.

2. Experimental design

The main objective of the experiments was to provide test cases for dispersion calculations of two-phase jets developing into plumes with passive dispersion. In order to develop a stage of passive dispersion within the boundaries of the test site, the release rates were set much lower than those in the Desert Tortoise experiments. The release durations were longer than those in other heavy-gas field experiments because we

wanted to obtain better statistics on concentration fluctuations. The ammonia source was designed to produce well-defined release conditions with reliable information on release rate, release momentum and thermodynamic state. Deposition of liquid aerosols was avoided by a sufficiently high exit pressure, since the average deposition rate would be difficult to measure and would introduce uncertainty in the downstream dispersion data. This choice may conflict with the interest in aerosol dynamics, but here priority was given to the dispersion aspect. The trials were limited to continuous jet releases in flat terrain without obstacles, and we did not attempt to measure fine details of near-source aerosol dynamics such as droplet size distribution and aerosol temperature deficit relative to the surrounding gas phase. The strong jet momentum affected most of the stage of dense gas spreading. We made use of all meterological conditions with reasonable wind directions and average wind speeds up to 6 m s^{-1}.

2.1. The test site

The experiments took place at the test site of Hydro-Care in Landskrona which is located in Sweden at latitude 55°53′ N, longitude 12°50′ E, at sea level. This site is currently used for practical training in mitigation of ammonia releases, and it was chosen in preference to a remote area because of the well-established security organization, workshop facilities, etc. Fig. 1 shows a map of the site with indications of measuring positions and a coordinate system aligned according to the sensor array. Also indicated on the map are surface characteristics and the height of upwind buildings. Because of the toxicity of ammonia the sensor array was aligned according to the wind direction which would transport the plume towards the water. This nearby water is a small cove and the open sea is behind an industrial area to the west of the test site. The release rate was restricted by the safety of a marina in the preferred downwind direction.

Measurements of local wind speeds show no systematic variation with downwind distance, but the turbulence level was higher near the upwind buildings. In order to assess the influence of the inhomogeneous turbulence field, the atmospheric dispersion model ADMS was used to calculate the dispersion of a plume of neutral buoyancy without initial momentum, see Edmunds and Britter [19]. This model predicted a significant building effect on 10 min average passive plume concentrations, especially in case of stable conditions. The building labelled 2 in Fig. 1 was identified as the main disturbance. For model comparison it is recommended to use the measured wind and turbulence fields rather than parameters of a surface layer in equilibrium. A surface roughness of $z_0 = 0.04$ m was evaluated from the 10 m mast in the middle of the field using average wind speeds at three heights and a situation with neutral atmospheric stability and wind coming from the unobstructed sector towards the water. This is a typical roughness length for tall grass and the distance from the shoreline ($x = 170$ m) should be sufficient to develop the internal boundary to the height of the mast ($h = 10$ m) according to the criterion

$$0.54x/h > \ln(h/z_0) - 1 \tag{1}$$

found in Panofsky and Dutton [20].

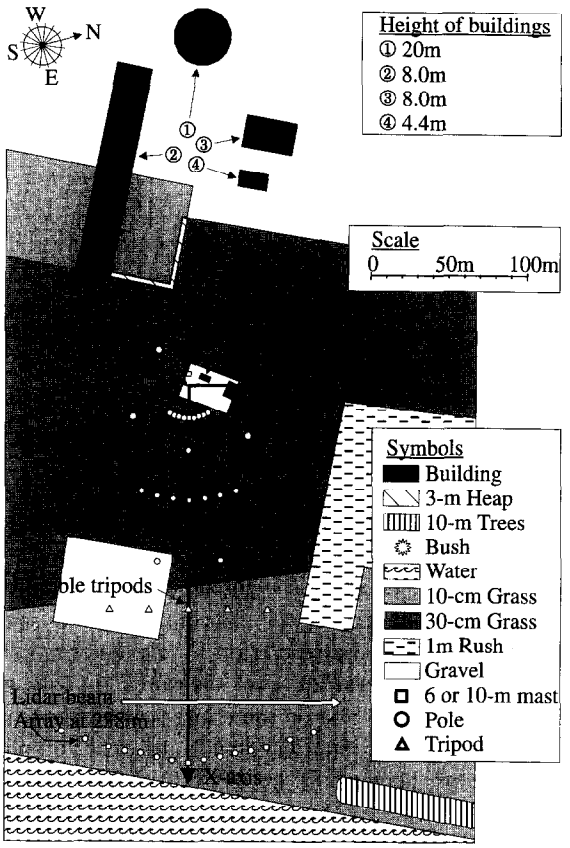

Fig. 1. Map of the test site including the array of measuring positions and a coordinate system aligned along the sensor array.

2.2. Sensor distribution

Sensors were mounted on five 10 m masts, a 6 m mast and the poles and tripods indicated on the map in Fig. 1. The choice of the subtended angle of such a sensor array is a dilemma; the spatial resolution will be reduced when distributing a fixed number of sensors over a wide angle, however a narrow angle will reduce the range of applicable wind directions. It was decided to distribute the sensors over a sector with an angle of 40°, i.e. giving priority to the spatial resolution. Apart from instruments near the source, the tripods shown at 150 m distance and the source itself, it was impossible to move the setup from day to day. We had to await the right wind conditions.

Most concentration sensors were distributed on three arcs at 20, 70, and 238 m from the ideal release point. The characteristic dispersion processes at these distances were intended to be a heavy jet, a near-neutral stage of transition and a fully developed passive plume, respectively. The distances were determined in the light of design calculations with the "box"-type GReAT model [21], observations during pilot experi-

ments in the first field campaign, and calculations based on the homogeneous equilibrium limit of the binary water–ammonia aerosol model of Vesala and Kukkonen [22]. The position of the second arc of sensors representing the stage of transition to passive dispersion was chosen according to a criterion for dense gas dispersion to dominate over passive dispersion, suggested by Britter and McQuaid [23]:

$$\sqrt[3]{\frac{\rho_{gas}-\rho_{air}}{\rho_{air}}\frac{g\dot{V}}{2\sigma_y u_{10}^3}} \leq 0.15 \tag{2}$$

Here ρ_{gas} and ρ_{air} are the source and air densities, $\dot{V}$ is the volumetric release rate, $2\sigma_y$ represents the local plume width and u_{10} is the wind velocity at 10 m height. The formula is applicable only for isothermal gas release, but in Section 3.2 we estimate the density effect of our two-phase ammonia release to be similar to that of an isothermal simulant gas with a molar weight of ~ 90 g mol^{-1}, i.e. 3.1 times that of air. This implies that the typical mass release rate of $\dot{m} = 0.25$ kg s^{-1} corresponds to an isothermal volumetric release rate of $\dot{V} \approx 0.067$ m^3 s^{-1}. With a plume width of $2\sigma_y \approx 15$ m, the Britter and McQauid transition criterion predicts dense gas dispersion effects at the second arc of sensors for wind speeds up to 3.0 m s^{-1}.

The first arc had sensors at two levels whereas the second and the third arcs had sensors at one level only. The reason for concentrating the sensors in these few horizontal chains was to obtain a good resolution for the determination of plume width and centre-line position. Vertical profiles were measured by four sensors on a single centre-line mast in the first two arcs and on three masts in the third arc. The three masts in the last arc were placed with a separation equal to the expected plume width with the intention that at least one of them would be exposed during the experiment. Most of these masts were 10 m high and they also carried meteorological equipment. Additional temperature measurements were made in the area just in front of the source. A meteorological reference mast was placed 7 m upwind of the source with the purpose of providing upwind boundary conditions for numerical models.

Table 1 gives an overview of the sensor distribution. The instruments were connected with micro-computers in the field, each measuring continuously and transmitting data to a master computer which logged all data. Drawings of the experimental layout, sensor specifications and details on data acquisition and processing are reported in Nielsen et al. [24].

2.3. Release system

The two-phase flashing ammonia jet was established by a movable source with mountable release nozzles. The release height was always 1.5 m above terrain and the jet was generally oriented in the horizontal downwind direction, except for a few releases with vertical jets. In order to minimize flow distortion of the ambient air flow the source was moved away from the storage tank and connected with a hose. The temperature of the storage tank was not controlled and therefore close to ambient temperature. The system was pressurized with nitrogen in order to reduce the likelihood of two-phase flow inside the release nozzle and to avoid pool formation in front of the source. The ammonia was extracted from the liquid phase at the bottom of the tank

Table 1
Distribution of instruments with downwind distance

Measurement	Instrument type	Number of instruments					
		−7 m	0 m	10 m	20 m	70 m	238 m
Pressure	Transducer		4				
Tank weight	Load cell		1				
Concentration	Catalytic				22	12	
	Electrochemical						22
	Uvic®						10[a]
	Sonic anemometer[b]				3		
	Lidar[c]						1[d]
Temperature	Thermocouple		2	64[a]	29		
Speed	Cup anemometer	3				3	5
Direction	Wind vane	1				1	2
Turbulence	Sonic anemometer	1				1	1
Humidity	Psychrometer	1					
Hum. and temp.	Solid state/Pt100	1			1	2	
Short wave radiation	Pyranometer	1					
	Albedometer[e]				1		
Long wave radiation	Pyrgeometer				1		
Surface temperature	Infrared[f]				1		
Air pressure	Barometer[g]	1					

[a] Occasionally re-arranged.
[b] Equipped with thermocouple.
[c] Beam across the plume.
[d] Only trials 23 and 25.
[e] Upward and downward pyranometer.
[f] Remote sensing.
[g] Solid state sensor.

through a siphon pipe, and the pressure was maintained by adding inert nitrogen gas at the top of the tank as sketched in Fig. 2. The ammonia tank and the nitrogen supply were placed on a load cell (Toledo) for an independent check of the released mass. For

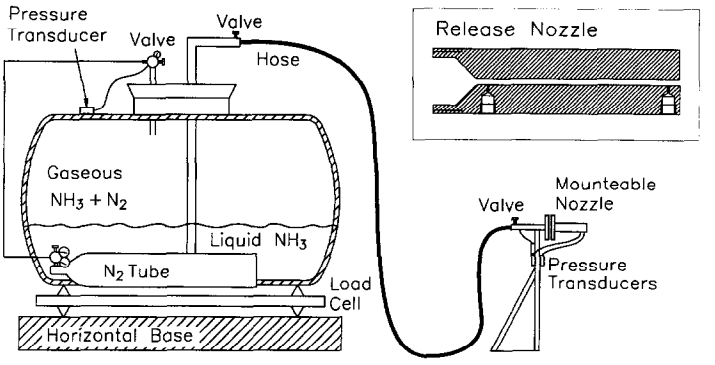

Fig. 2. The release system consisting of a tank with pressurized liquid ammonia connected to a movable source with mountable nozzles. The nozzle design is shown at the top right corner.

security reasons we used the control valve at the top of the tank and emptied the hose after each trial. The shut-down process involved an O(30) s period of a not very well defined two-phase flow with decreasing liquid fraction in the release nozzle.

The chosen release conditions are representative for accidents from small tanks used for transport or as storage for ordinary consumers. Large storages, e.g. at a manufacturer, are sometimes semi or fully refrigerated, and accidental releases from these will result in jets with less flash evaporation or cryogenic pools, respectively.

Three release nozzles with different diameters and nominal release rates of 0.1, 0.2 and 0.5 kg s^{-1} were manufactured. The top right part of Fig. 2 shows the mountable part of the medium-sized 4 mm nozzle, where the flow direction is from left to right through a 45° conical contraction with smoothed edges. Measuring channels and fittings for connections to pressure transducers (Valcom) were drilled just downstream of the nozzle contraction and near the outlet. Connections between the measuring points and the pressure transducers were filled with silicon oil and care was taken to avoid air bubbles. Similar pressure measurements were made in the permanent part of the source just upstream of the contraction and in the gas phase of the release tank. The nozzle temperature T_0 was measured just upstream of the contraction by a Pt100 thermometer placed in a thin probe within the pipe.

Artificially generated smoke was applied in experiments with Lidar measurements. An aerosol generator produced a continuous release of submicron particles consisting of a conglomerate of SiO_2 and NH_4Cl which could be detected by the Lidar system. Mixing liquid $SiCl_4$ and 25% aqueous NH_4OH in a neutralizing stoichiometric ratio (1 : 3.2), the reactions between the two liquids were as follows:

$$SiCl_4 + 2H_2O \rightarrow SiO_2 + 4HCl$$

$$NH_4OH + HCl \rightarrow NH_4Cl + H_2O$$

The flow of chemicals was kept at a constant rate, and the plumes were visible even downwind of the test area. The two liquids were mixed in a fan mounted on top of the regular ammonia source and the smoke was entrained into the flashing ammonia jet. Earlier experiments have shown the smoke particle size distribution to be log-normal with an average radius of 0.23 μm. The solid smoke particles probably served as condensation nuclei for liquid aerosols, perhaps changing the aerosol dynamics in the two Lidar experiments, but aerosol rain-out had an insignificant effect on the overall plume mass balance. The assumed proportionality between Lidar signal and ammonia concentration relies on three hypotheses: proportional ammonia and smoke release rates, homogeneous mixing near the source, and spatially independent smoke particle size distribution. The mass of the added smoke particles was ~ 2% of the mass of the released amount of ammonia. The momentum of the air fan is not accurately known but estimated to ~ 50% of the flashing jet flow force.

2.4. Concentration measurements

In the following we first review the technical requirements for the concentration sensors and then describe the chosen instrumentation. Our purpose was to measure the plume dimensions and to study the concentration fluctuations and this leads to different demands on the sensor response times. Spectral analysis of concentration data from the

previous propane experiments [25] had shown that the typical peak in the power spectra was near 1 Hz, and in order to detect at least one decade of the inertial subrange the time response of the sensors for detection of concentration fluctuations had to be better than 10 Hz. Determination of plume dimensions did not require equally fast-responding sensors. We did, however, plan to detect the plume position which was expected to meander with a time scale of 5 s near the first arc of sensors and 20 s near the last arc of sensors, and the slow responding sensors should be able to follow this process. Given the uncertainty in state-of-the-art dispersion models, there was no need for extremely accurate sensors, although it was desirable to detect the shape of concentration profiles leading to a demand of $\sim 10\%$ relative accuracy. A particular aspect of a two-phase release is that part of the contaminant may be transported in the liquid aerosol phase, and for this reason Goldwire et al. [16] pumped a sample flow through a heating device before measuring the bulk concentration. This was not found necessary in our case since the liquid ammonia fraction was expected to be small at the measuring points and the gas-phase concentration would therefore be representative for the two-phase mixture. In the Appendix we estimate the liquid ammonia fraction to be 2% at this distance giving errors of measurement which are less than the sensor accuracy.

Three types of concentration sensors were applied in the experiments. Their principles of operation were catalytic combustion, electrochemical cells and ionization by ultra-violet light. Additional concentration estimates were obtained from sonic anemometers equipped with thermocouples and by a back-scatter Lidar. Their downwind distribution is shown in Table 1.

The catalytic concentration sensor (Dräger Polytron Ex) was the main device to detect the plume shape and position in the first two arcs of sensors. The majority of sensors in the previous MTH Project BA propane experiments [7] worked on the same measuring principle and the response time of the instrument was similar, i.e. O(5) s. The gas entered the catalytic reaction chamber through a porous membrane in a sensor head which pointed downward and shielded the membrane from direct impaction by liquid aerosols. The instruments were calibrated in situ using a reference gas with known concentration. The response time of each sensor was deduced from the individual calibration signals, and numerical response enhancement was applied as explained in the design report of Nielsen et al. [24]. This speed-up method has a tendency to enhance random noise, so both the original and the "improved" signals are made accessible. The catalytic sensors were known to be sensitive to ambient conditions like temperature, humidity and pressure. These systematic errors resulted in signal offsets which were corrected later on, setting the pretrial concentration to zero. After exposure to high gas concentration, a steady slightly negative signal ($\sim 5\%$ of the previous maximum signal), was occasionally emitted for a period of a few minutes. No correction of this error was attempted.

The electrochemical cell sensor (Dräger Polytron NH_3) detected the plume shape and position in the domain of low concentration in the third arc. The measuring principle of this device is similar to that of the oxygen deficit sensors applied in the Thorney Island experiments, see Leck and Lowe [26], but the response is slower since the ammonia sensor had no built-in electronic response enhancement or aspiration. The response function was examined as for the catalytic sensors and was found to have a long tail

which probably resulted from diffusion in the electrochemical cell. This response function is not a linear autoregressive process, but it may be approximated by a sum of two exponential functions allowing us to filter the long tail leaving the processed signals with first-order response times O(15) s, see Nielsen et al. [24]. The sensor had base-line drift and slightly negative posttrial signals very similar to those of the catalytic sensors.

The fast Uvic® sensor had a better response than 20 Hz which makes it ideal for measurements of concentration fluctuations. The instrument detects any gas which is ionized by ultra-violet light including ammonia. In Landskrona the background signal was found to be insignificant compared to the relevant range of ammonia detection. It was possible to apply the Uvic® sensor up to ~ 2000 ppm using the unlinear calibration curve described in Nyrén et al. [27]. A calibration curve for each campaign and each sensor was established by reference measurements of several premixed ammonia concentrations. The Uvic® sensors were mounted either on the centre-line mast at 238 m distance or on tripods arranged in various configurations 150 m from the source and further downstream.

Additional concentration estimates were deduced from sonic anemometers (Kaijo Denki) with attached thermocouples at 20 m distance. A sonic anemometer detects the speed of sound

$$\sqrt{\frac{c_p RT}{c_v M_{\text{air}}}}$$

and derives the sound virtual temperature T, as if the mixture heat capacities c_p, c_v and molar weight M_{air} were those of atmospheric air. These gas properties change when a foreign compound is part of the mixture, and the sound virtual temperature will differ from the true temperature measured by the attached thermocouple. It is possible to derive the gas concentration from this temperature difference by a technique which worked quite well in the previous propane experiments, see Nielsen [28]. The gas-induced response of the sound virtual temperature of the sonic anemometers is however much smaller when exposed to ammonia than to propane and the derived concentration time series had to be smoothed with a 1 s moving average filter, in order to improve the unfavourable signal-to-noise ratio. Therefore the ammonia concentration estimates by the sonic/thermocouple method are not adequate to detect concentration fluctuations although they are faster than measurements by the nearby catalytic concentration sensors.

Two trials included concentration measurements with a mini-Lidar (Risø). This instrument fires a short pulse of laser light and detects the range and intensity of the reflection from airborne particles. The Lidar was operated 220 m downstream of the source. At this distance the plume was normally invisible, and so artificial smoke was added to the ammonia plume during these particular trials. The particle size distribution of the smoke is known to be nearly independent of the dilution factor and the initial mixing of smoke and gas seemed to be efficient. With a small correction for reflectivity of the background atmosphere, the detected light reflection is proportional to the particle concentration, which in turn is assumed to be proportional to ammonia concentration, see above. The measuring path was projected across the plume at 2 m height, and laser

pulses were emitted with intervals of 3 sec giving instantaneous line profiles of relative concentration with a spatial resolution of 1.2 m along the measuring path. At the plume position the diameter of the laser beam was ~ 0.5 m. The data were processed using optical parameters of the artificial smoke, the typical background atmosphere and the Lidar system itself as determined in previous calibration experiments by Jorgensen et al. [29]. The background particle concentrations outside the plume were insignificant.

2.5. Temperature measurements

The gas concentration was expected to be correlated by a temperature drop caused by the initial enthalpy deficit. A thermocouple was mounted next to each gas sensor in the arc 20 m from the source in order to detect whether the local concentration and temperature signals were in accordance with an assumption of perfect adiabatic mixing with the ambient air. Further downstream the plume temperature deficit was expected to be insignificant compared to the background temperature fluctuations and no thermocouples were mounted in the second or third arc of sensors. In the first pilot field campaign an additional fine mesh of 8×8 thermocouples were mounted on a rig placed 2–5 m in front of the source. The intention was to measure the temperature field across the two-phase jet as in a previous flame experiment by Ott [30]. To our surprise the thin thermocouple wires provoked a lot of ice deposition, and we found that the signals soon approached the constant temperature of the deposit instead of the variable temperature field of the jet. In the subsequent campaigns some of these thermocouples were therefore redistributed on a 2 m minimast and on horizontal strings in the area 10–20 m from the source. The deposition rate was smaller at these distances, but presumably they caused too low temperature measurements just after gas exposure and during quiescent periods when the jet moved away from the individual sensor. In a sense this was not an instrumental error, but the measured temperature did not represent the surrounding gas-phase temperature while the probes were wet and the gas-phase temperature was above the dew point. Inside the jet, where the temperature was below the dew point, the measurements are assumed to be correct. During the data collection of Nielsen and Ott [31] this thermocouple problems was observed in every liquefied gas experiment including Desert Tortoise (see the plots in Goldwire et al. [16]).

2.6. Meteorological measurements

Participants of the main Fladis project asked for data on the upwind flow profile which was an important boundary condition for numerical and wind-tunnel models. More meteorological masts were added since the short-term average wind direction was expected to change with downstream distance, and the shelter from the upwind buildings might influence the local flow and turbulence. The wind field was measured by three cup anemometers (Risø) and a wind vane (Risø) mounted on the centre-line 10 m masts except at 20 m distance, where we were anxious about the corrosive effect of ammonia mentioned by Goldwire et al. [16]. The 10 m masts at the edges of the arc at 238 m distance carried only one cup anemometer each. The atmospheric turbulence was

measured by ultrasonic anemometers (Solent) at 4 m height mounted on the upstream reference mast and on the centre-line masts at 70 and 238 m distance. The measured effect of upwind buildings is discussed above.

Air humidity was measured by an automatic psychrometer (Frankenberger) at the upstream reference mast. Additional solid state humidity sensors (Vaisala) were distributed at the centre-line masts of the first and the second sensor arrays and for comparison next to the upstream psychrometer. Atmospheric short- and long-wave radiation sensors (Kipp and Zonen) were mounted at 20 m distance and the atmospheric pressure was measured by a barometer (Vaisala) inside a cabin. Information on heat flux from the ground to the cold ammonia plume was desirable but difficult to obtain. As a substitute a remote sensing infrared thermometer (Hiemann) was mounted on the top of the 6 m mast at 20 m distance and directed toward the ground 18 m downstream of the source. The surface temperature measured by this instrument is only reliable before and after each trial owing to obscuration by aerosols in the plume.

2.7. Aerosol samples

An attempt to measure the concentration by a catalytic sensor 4 m downstream of the source was no success. The instrument was covered by a thick layer of water/ammonia deposit and measured ammonia for hours after the actual release. Every obstacle as close as ~ 10 m to the source was covered by this deposit, especially in case of high air humidity. It was decided to collect samples of this deposit in order to analyze the composition. The collectors were made from ordinary aluminium foil folded to an envelope with a weight less than 1 g and a capacity for 20 g of liquid. The envelopes were placed on pieces of steel wire mounted on small movable masts following the height of the jet centre-line. The envelopes were collected immediately after each trial and dropped into bottles containing known amounts of pure water. The bottles were sealed and stored in a refrigerator before analysis in order to reduce the rate of ammonia evaporation from the sample. The ammonia content of each sample was determined from the concentration in the bottle and from the weight of the sample and water originally in the bottle.

3. Description of the experiments

3.1. Release conditions

Three field campaigns with a total number of 27 trials were conducted. Data from pilot tests and trials with obviously bad wind conditions or unsuccessful data acquisition have not been processed, and this limits the set of processed data to 16 experiments. Table 2 provides an overview of release conditions for these and adequate input data for most heavy-gas dispersion models. The exit pressure p_0 is measured two nozzle diameters from the outlet whereas T_0 is the temperature measured upstream of the nozzle contraction. The release rate $\dot{m}$ is calculated from the pressure drop through the conical nozzle contraction where the flow was in liquid phase. The time integral of this

Table 2
Overview of release conditions

Trial	Date	Time	Ø	∠	p_0	T_0	$\dot{m}$	F_{jet}	M_{eff}	T_{dur}	u_{10}	Δ_{Dir}	σ_u	σ_{Dir}	u_*	L	p_{air}	T_{air}	R.H.	$I_\downarrow$
6	7/4/93	13:25	6.3	→	5.9	7	0.42	24	92	10	2.7	2	0.64	18.5	0.36	−51	–	9	67	–
7	7/4/93	14:00	6.3	→	5.7	7	0.42	24	92	5	2.9	4	0.62	18.7	0.34	−28	–	8	57	–
9	7/8/93	14:39	6.3	→	6.9	14	0.40	27	89	15	6.1	5	1.35	12.3	0.44	348	1020	16	86	131
12	10/8/93	15:31	4.0	↑	7.2	16	0.20	13	88	5	2.2	−7	0.57	14.2	0.15	−61	999	16	75	247
13	11/8/93	14:25	6.3	→	7.7	18	0.50	34	87	15	5.5	−27	1.03	9.5	0.48	−164	1008	16	52	653
14	11/8/93	15:51	6.3	→	7.4	17	0.47	32	88	10	5.2	−31	1.15	11.7	0.45	−174	1008	17	53	509
15	13/8/93	19:18	6.3	→	7.7	18	0.51	34	87	3	5.9	−7	0.91	8.0	0.50	271	1019	17	60	134
16	13/8/93	19:51	4.0	→	8.0	17	0.27	18	88	20	4.4	−8	0.87	9.6	0.41	138	1020	16	62	85
17	13/8/93	21:09	4.0	→	7.9	15	0.27	18	88	25	3.7	−28	0.72	9.6	0.31	59	1020	16	63	0
20	23/8/94	12:29	4.0	→	7.9	16	0.23	15	88	40	4.0	−7	0.70	12.8	0.38	−25	1018	20	69	660
21	23/8/94	16:50	6.3	→	6.5	12	0.57	29	89	40	4.3	24	0.78	10.0	0.34	−53	1017	21	59	390
23	30/8/94	11:56	6.3	→	7.6	16	0.43	28	88	20	6.6	−7	1.24	9.5	0.53	−112	1012	17	54	674
24	30/8/94	16:06	6.3	→	5.7	9	0.46	18	90	10	4.9	−6	0.84	9.7	0.41	−77	1013	18	54	448
25	30/8/94	16:38	6.3	→	5.9	9	0.46	21	90	22	4.5	−6	0.87	11.8	0.43	−201	1013	17	54	239
26	31/8/94	14:49	4.0	→	8.3	20	0.21	12	86	10	3.0	−31	0.48	13.6	0.29	−16	1019	19	52	606
27	31/8/94	16:41	4.0	→	8.5	20	0.22	13	86	21	2.4	−10	0.51	19.6	0.25	−22	1019	19	50	326

All parameters are calculated over the release period of each trial and the standard deviations of wind speed and direction are therefore not directly comparable. The wind direction is measured at 10 m height, except in trials 6 and 7 (campaign 1) where it has been measured at the 4 m level.

Time = Start of release.
Ø = Nozzle diameter (mm).
∠ = Jet direction.
p_0 = Exit pressure (bar).
T_0 = Nozzle temperature (°C).
$\dot{m}$ = Release rate (kg s^{-1}).
F_{jet} = Jet flow force (N).
M_{eff} = "Effective" molar weight (g mol^{-1}).
T_{dur} = Release duration (min).
u_{10} = Average wind speed at 10 m (m s^{-1}).
Δ_{Dir} = Wind direction relative to ideal (deg).
σ_u = Standard deviation of wind speed (m s^{-1}).
σ_{Dir} = Standard deviation of wind direction (deg).
u_* = Friction velocity (m s^{-1})
L = Monin–Obukhov length (m).
p_{air} = Atmospheric pressure (mbar).
T_{air} = Ambient temperature (°C).
R.H. = Relative humidity (%).
$I_\downarrow$ = Insolation (W m^{-2}).

is slightly less than the corresponding weight loss of the ammonia tank with an average disagreement of 2% for the 4 mm nozzle and 5% for the 6.3 mm nozzle. The jet flow force F_{jet} and the "effective" molar weight M_{eff} will be defined below.

The wind speed u_{10} and wind direction Δ_{Dir} relative to the one preferred are average values of measurements from four masts in the field. Their standard deviations σ_u and σ_{Dir} are calculated as the mean of the local standard deviations, i.e. the contribution from spatial variation of the mean values is not included. The friction velocity u_* and the Monin–Obukhov length L are based on measurements by the sonic anemometer at

the 4 m level of the upstream reference mast. The turbulent fluxes are found by eddy correlation of time series which are transformed to a coordinate system aligned according to the local wind vector. Because of the upwind buildings the average flow profile is not in equilibrium with the turbulence at the reference mast. The magnitude of the deviation may be evaluated by comparison with the log–linear flow profile for an equilibrium boundary layer:

$$u(z) = \frac{u_*}{\kappa}\left[\ln\frac{z}{z_0} + \psi_m\left(\frac{z}{L}\right)\right] \tag{3}$$

Here, $\kappa = 0.4$ is the von Karman constant, and Ψ_m is an empirical diabatic correction function, see Paulson [32]. When inserting the measured turbulence parameters u_* and L, and the estimated surface roughness of $z_0 = 0.04$ m we obtain velocities which on the average are 15% and sometimes considerably more in excess of the real velocity. Additional turbulence data are available from the sonic anemometers at 70 and 238 m distance, and it is recommended to use these measurements rather than equilibrium boundary layer theory. Model users in need of a Pasquill–Turner stability class may interpret the measured Monin–Obukhov length L by a Golder diagram [33]. The ambient temperature T_a, relative humidity R.H. and short-wave downward radiation $I_\downarrow$ are measured at the 1.5 m level of the upstream reference mast.

All parameters are averaged over the individual release period of each trial. It may be argued that stable statistics of the friction velocity u_* and the Monin–Obukhov length scale L require longer average periods than those in some of our trials, but it was felt that also these parameters should represent the actual release period. The spectral representation of the horizontal wind speeds contains significant variability on time scales ~ 10 min, see Panofsky and Dutton [2]. Short observation periods will remove part of this variability, and the different duration of individual experiments imply that the presented standard deviations of wind speed and direction are not directly comparable.

Table 3 contains a brief characteristic of each trial. Experiments with long release durations and good average wind directions should be of greater interest for analysis. In principle trials with short release duration could provide interesting information on longitudinal cloud dispersion like the recent experiments at the Nevada test site, see Hanna [34]. Our instrumentation did however involve sensors with slow response times and the source had a finite shut-down time. In selecting experiments for analysis it should be noted that trials 6 and 7 used a limited instrumentation during the first field campaign and that the durations of trial 12 and 15 were relatively short. We made a variable deployment of the fast Uvic® concentration sensors, near-source thermometers and aerosol samplers, and the Lidar instruments were applied only in trials 23 and 25. The vertical jet source of trial 12 makes this release different from the rest. A further description of each experiment is given in electronic text files distributed together with the data, see below.

3.2. Source diagnostics

The exit pressure p_0, i.e. the measurement at the tip of the nozzle and the nozzle temperature T_0 are directly applicable as input to a numerical dispersion model with a

Table 3
Comments on individual releases

Trial	Comments
6	Good wind condition, but limited instrumentation
7	As for trial 6
9	A drizzle just stopped and the ground was wet, but apparently the measurements were not disturbed by moisture; gradually shifting wind direction
12	Vertical release
13	Poor wind direction, low air humidity
14	As for trial 13
15	Good wind direction; interrupted for security reasons
16	Best trial in the second campaign, analyzed by participants of the main Fladis project
17	Less ideal wind direction than that of trial 16, stable atmosphere
20	Good average wind direction, but sometimes the plume was too far to the left-hand side; Uvic® concentration sensors placed in a close formation
21	Plume close to the right-hand edge of the sensor array
23	Good average wind direction, but sometimes the plume was too far to the left hand side; artificial smoke added to the plume and detected by a Lidar system
24	Good wind direction
25	Artificial smoke and Lidar as in trial 23
26	Unfavourable wind direction, low wind speed
27	Low wind speed and highly variable wind direction, low humidity

built-in source module. Estimates of the source dynamics will be of greater interest to other purposes, e.g. wind-tunnel modelling.

The first step in the source diagnostic is to check the thermodynamic state of the emission. In about half of the trials (trials 12–15, 24, and 26) the boiling point corresponding to the exit pressure $T_{\text{boil}}(p_0)$ was slightly less than the temperature measured near the nozzle contraction T_0. This indicates the beginning of a two-phase flow near the outlet, and the outlet liquid fraction by mass α may be estimated by the simple enthalpy balance

$$\Delta L_{\text{NH}_3}(1-\alpha) = c_{\text{liq}}[T_0 - T_{\text{boil}}(p_0)] \tag{4}$$

where c_{liq} is the liquid heat capacity and ΔL_{NH_3} is the latent heat of ammonia vaporization. The temperature drop was O(1)°C and the maximum vapour fraction was O(1)%. The small initial vapour fraction reduces the jet flow force which is estimated by the model of Nyrén and Winter [35]

$$F_{\text{jet}} \approx \frac{\dot{m}^2}{A}\left(\frac{(1-\alpha)RT_{\text{boil}}(p_0)}{Mp_0} + \frac{\alpha}{\rho_{\text{liq}}(T_0)}\right) + (p_0 - p_{\text{air}})A \tag{5}$$

where A is the nozzle cross section, R is the universal gas constant, ρ_{liq} is liquid density and p_{air} is ambient pressure. The unknown velocity distribution of the flow is neglected.

The "effective" molar weight M_{eff} is used as a simple way to characterize the approximate density effect. The background for this concept is a discussion among participants of the main Fladis project on how to model two-phase releases with

isothermal model gas. Model experiments with an isothermal simulant gas with M_{eff} approximates the density of a two-phase release after aerosol evaporation. This "effective" molar weight is calculated by

$$M_{\text{eff}} = M - \frac{\Delta H_0}{c_p^{\text{air}} T_{\text{air}}} \tag{6}$$

where ΔH_0 is the enthalpy difference between the contaminant of source and ambient conditions. This is derived in the Appendix to this article which includes comparisons with more accurate two-phase density calculations. The M_{eff} approximation is not valid for high aerosol loads, and at worst (near the first sensor array in trial 9) it results in a 78% overprediction of the density difference relative to the ambient $\Delta\rho$. The deviations are less severe for other trials and often limited to the near-source area where jet momentum dominates the dispersion process.

3.3. Data distribution

The data base was organized to match the needs of the main Fladis project. In practice this meant a hierarchy of information with different degrees of detail since some researchers asked for complete time series whereas other wanted data analyses like "average surface concentration at the plume centre-line". It was pointed out that background information, e.g. accurate sensor positions, should be accessible.

The available information includes measured time series, block statistics, written documentation and a set of utility programs. All successful measurements are included with corrections for unlinear sensor response and known errors as reported by Nielsen et al. [24]. A set of 1 min block statistics written as comma-separated files may easily be imported into commercial database, plotting or spreadsheet programs. The documentation was divided into general notes and notes on individual trials. The general information include descriptions of surface roughness, instrument response times and drawings. The volume of the specific information vary, but a description of release conditions, source position and a list of signals are repeated for each trial. The signal list provides information on sensor position, sample frequency, measured property, physical unit and a short comment like "a slight noise from . . ."or simply "ok".

Utility programs were distributed with the data and accessed through a program shell. Groups of time series, e.g. signals from a row of sensors, may be plotted on a PC screen or exported to *hpgl* and *postscript* graphics. More than 700 of these plots have been predefined and each of them is accompanied by written comments. This system is intended to substitute a lengthy data report and our visual inspection of the time series is a good check of the measurement quality. The user may calculate average profiles and probability density functions in selected periods and translate binary time series to *ascii* files. Computer animations show the variable concentration field, sequences of Lidar profiles, wind trajectories and the concept of moving-frame profile analysis.

The information is prepared for FTP distribution (for free) and also available on CD-ROM and Magneto-Optical disks (with a distribution charge). The volume of the

installed system is 122 MB distributed on 20740 MS-DOS files. Further details are found on the Internet at

http://www.risoe.dk/amv/atu/densegas

4. Plume dimensions

Concepts like centre-line concentration, plume height and plume width were needed for comparison with dispersion models and wind-tunnel simulations. The aim of this section is to deduce these plume characteristics from the available point measurements.

4.1. Horizontal profiles

Unlike a wind-tunnel simulation the atmospheric wind direction and plume centre-line position are not known a priori but have to be determined by observation. Long-time average plume positions should be in accordance with average wind directions. However in case of short averaging times it becomes increasingly difficult to correlate local wind directions to the plume position, which is determined by a time history of wind directions along the plume trajectory. Therefore it is better to determine also the plume position from concentration measurements. At this point of the analysis one may choose either to start calculating local average concentrations and then fit the average concentration profile or, alternatively, to find instantaneous plume positions and then calculate plume statistics in a frame of reference following the moving plume centre-line. In the following we shall apply both methods. From a risk analysis point of view it may be more relevant to know a typical instantaneous plume profile than the average of a meandering plume. The plume dimensions predicted by most dense gas dispersion models are presumably consistent with average concentrations without plume meandering. The moving-frame analysis should therefore be of greater interest in the heavy-gas phase. However a longer averaging time, e.g. 10 min, is usual in dispersion models for passive diffusion, and many heavy-gas models are designed with a smooth transition to this limit. The best data analysis for a model comparison depends on the individual model assumptions. The wind direction in wind tunnels is more steady than in the atmosphere, and the result of the moving-frame analysis is expected to better compare to laboratory measurements. The data reduction for the heavy-gas model evaluation of Hanna et al. [36] applied fixed-frame statistics. An experiment like Fladis trial 9 would probably have been rejected by these authors, since the varying wind direction during this trial resulted in a very broad fixed-frame profile. On the other hand, the moving-frame profile from such a trial will still be useful. The concept of a meandering plume has previously been used to predict concentration fluctuations in plumes of neutral buoyancy, see Wilson [37] for an introduction.

Fig. 3 shows a set of concentration time series from the lowest level of the first sensor array which in this trial was 22 m downstream of the release point. The variable plume position and width are shown in the map above the concentration time series. The release continued for 20 min and the plume was sweeping from side to side with about

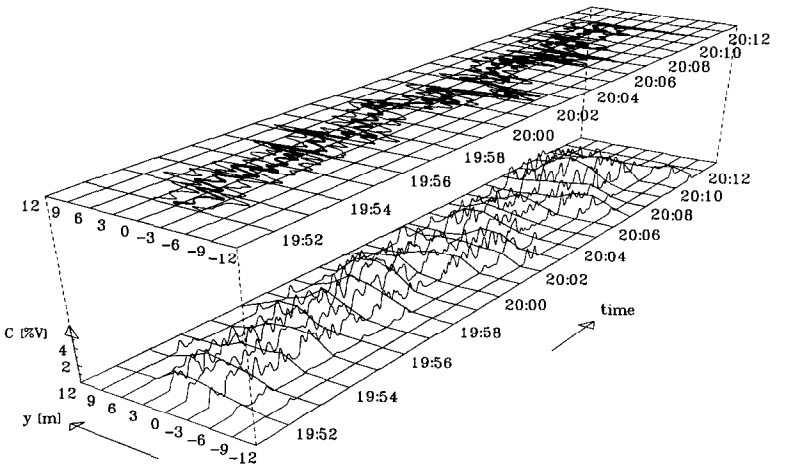

Fig. 3. Concentration time series from trial 16. The map above the series shows the position of the instantaneous plume centre-line y_c (thick line) and the lateral plume spreading $y_c \pm \sigma_y$ (normal line) as a function of time.

two excursions per minute. Signals from adjacent sensors are well correlated and it seems as if much of the concentration fluctuation was caused by the variable plume position.

The average and standard deviation of each signal from Fig. 3 are plotted in the lower left frame of Fig. 4 and similar data from other chains of sensors are plotted above this. The Gaussian profiles fitted to each chain of measurements seem to describe the horizontal concentration distribution quite well.

The instantaneous concentration profiles were of a variable shape, and each profile is therefore approximated by a stepwise linear variation between neighbouring measurements

$$c(y) \approx \frac{c_{i+1}(y - y_i) + c_i(y_{i+1} - y)}{y_{i+1} - y_i} \quad \text{for } y_i < y < y_{i+1} \tag{7}$$

and set to zero outside the sensor array. The instantaneous position of the centre-line is taken as the centroid of this distribution

$$y_c = \frac{\sum_{i=1}^{I-1} \int_{y_i}^{y_{i+1}} c(y)\, y\, \mathrm{d}y}{\sum_{i=1}^{I-1} \int_{y_i}^{y_{i+1}} c(y)\, \mathrm{d}y} \tag{8}$$

The estimate implicitly assumes that the concentrations at the edges are insignificant $c(y)y \to 0$, since otherwise the estimated y_c would be biased toward the ideal centre-line. The assumption was not always valid and this source of error will be evaluated below. Another problem is to what extent the concentration signals should be smoothed before determination of the plume position. Random fluctuations in a finite number of signals could introduce uncertainties in the plume position y_c, but too much smoothing would bias y_c toward the ideal centre-line. The concentration signals were obtained by rather

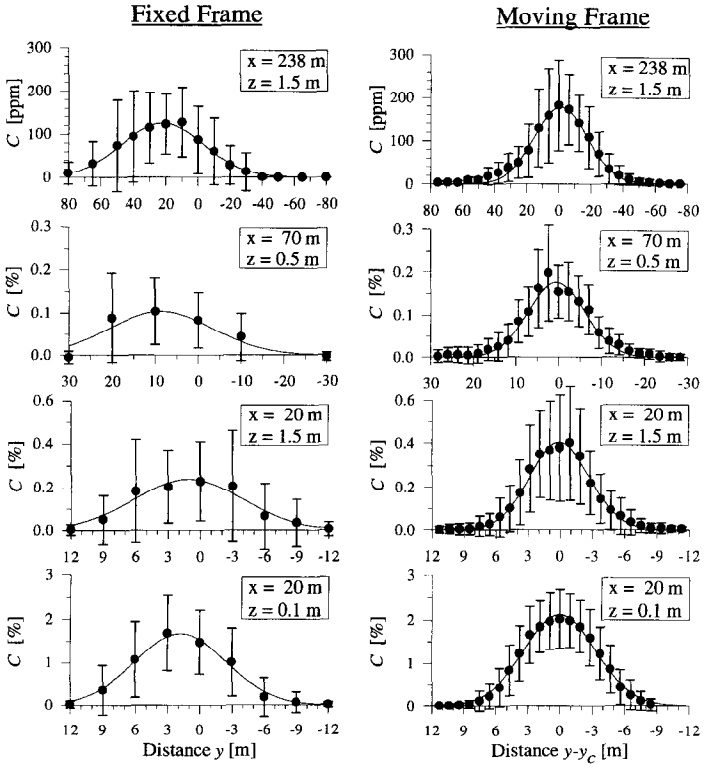

Fig. 4. Horizontal average concentration profiles in trial 16 plotted in (1) a fixed frame of reference, and (2) a moving frame of reference following the instantaneous plume centre-line position y_c.

slowly responding sensors, so the instantaneous centre-line position has actually been estimated by the speed-up signals, i.e. with ~ 5 s response time for the sensors in the measuring arrays at 20 and 70 m distance and ~ 15 s at 238 m distance.

The plots on the right-hand side of Fig. 4 apply a moving frame of reference, where the observations are sorted in bins defined from the distance between the sensor position and instantaneous plume centre-line $y - y_c$. The number of bins is an arbitrary choice. As expected the moving-frame profiles are more narrow with higher maximum concentrations than the fixed-frame profiles. The intensity of the concentration fluctuations σ_c/μ_c is smaller in the moving-frame profiles, i.e. the concentration is more predictable with a known plume centre-line. In trials with short release durations the moving-frame profiles are often more symmetric than the fixed-frame profiles. This indicates less statistical uncertainty since presumably the mixing process is symmetric. In the two moving-frame profiles of the first sensor array the jet is seen to be wider near the ground. The reason could be gas which lingers near the surface each time the core of the jet is swept to the other side.

The estimated Gaussian curves in Fig. 4 are derived from an iteration which compares the moments of the stepwise linear profile to moments of a clipped Gaussian

Table 4
Centre-line concentration c_{max}, plume spreading σ_y, and vertical centre of gravity $\bar{z}_{est}$ with the correction $\Delta\bar{z}_{est}$ at distance x_r and height z_r

	x_r (m)	z_r (m)	$c_{max}(x_r, z_r)$ (ppm)	$\sigma_y(x_r, z_r)$ (m)	$\bar{z}_{est} + \Delta\bar{z}_{est}$(m)	T_{obs} / T_{dur}
Trial 9	20	0.1	19600 (12800)	2.66 (4.08)	0.95 + 0.11/0.05	1.03
	70	0.5	2050 (885)	5.70 (15.5)	3.32 + 0.53/0.29	1.03
	238	1.5	138 (57)	13.6 (37.6)	?	1.04
Trial 12	16	0.1	10300 (7740)	4.03 (5.04)	?	< 1
(vertical)	66	0.5	1180 (1010)	12.6 (16.1)	2.65 + 0.27/0.12	1.03
Trial 13	22	0.1	24800 (21200)	3.53 (4.03)	0.91 + 0.10/0.05	< 1
Trial 14	22	0.1	24000 (20700)	3.50 (3.93)	0.92 + 0.10/0.04	1.06
Trial 15	22	0.1	26200 (20700)	2.90 (3.58)	0.85 + 0.08/0.03	1.08
	72	0.5	2360 (1710)	7.21 (10.3)	2.45 + 0.20/0.07	1.06
	240	1.5	166(127)	19.0 (26.9)	?	1.28
Trial 16	22	0.1	21300 (16700)	3.38 (4.27)	0.83 + 0.07/0.03	< 1
	72	0.5	1810 (1090)	6.77 (11.7)	2.62 + 0.26/0.11	< 1
	240	1.5	179 (127)	16.7 (25.3)	?	1.05
Trial 17	22	0.1	19200 (16900)	3.54 (3.88)	0.83 + 0.07/0.03	1.06
	72	0.5	1570 (1380)	7.68 (7.26)	3.66 + 0.70/0.42	< 1
Trial 20	20	0.1	21600 (12900)	3.00 (4.84)	0.78 + 0.06/0.02	1.02
	70	0.5	1140 (583)	8.86 (18.6)	3.21 + 0.48/0.25	< 1
Trial 21	20	0.1	37600 (30100)	3.05 (3.72)	0.78 + 0.06/0.02	1.01
	70	0.5	5910 (3600)	7.86 (12.9)	1.85 + 0.06/0.01	1.02
Trial 23	20	0.1	20400 (15100)	2.46 (3.22)	0.91 + 0.10/0.05	1.03
	70	0.5	1880 (1250)	6.97 (10.4)	2.50 + 0.22/0.09	1.02
	238	1.5	92 (62)	20.7 (31.9)	?	1.02
Trial 24	20	0.1	31700 (26400)	3.21 (3.65)	0.77 + 0.06/0.02	1.08
	70	0.5	2560 (1690)	8.57 (14.0)	2.59 + 0.25/0.10	1.08
	238	1.5	113 (74)	24.7 (40.2)	?	1.13
Trial 25	20	0.1	33700 (29000)	3.30 (3.59)	0.76 + 0.05/0.02	1.03
	70	0.5	3270 (2040)	7.73 (12.6)	2.00 + 0.09/0.02	1.00
	238	1.5	146 (98)	21.3 (32.9)	?	1.03
Trial 27	20	0.1	25200 (19500)	4.60 (5.54)	0.62 + 0.02/0.00	1.07
	70	0.5	1850 (951)	8.60 (16.3)	2.58 + 0.25/0.10	1.08

The primary values of the c_{max} and σ_y parameters correspond to measurements in a moving frame of reference, whereas the values in parentheses are found from the same measurements in a fixed frame of reference. The two values of the $\Delta\bar{z}_{est}$ corrections are for $c \propto \exp(-z)$ and $c \propto \exp(-z^{3/2})$ respectively. The ratio of the individual observation period T_{obs} and release duration T_{dur} is shown in the last column.

distribution, see Nielsen [38]. In order to avoid the effect of the poor sinal-to-noise ratios at the edges of the distribution, the iteration disregards signals from sensors which are more than two standard deviations from the predicted plume centre-line. The centre-line concentration c_{max} and plume spreading σ_y for the fitted profiles are listed in Table 4. Here the primary values are found from curve fits to moving-frame profiles and the values in parentheses are from fixed-frame profiles. In some trials part of the plume occasionally appeared outside the measuring array. This gave rise to uncertain estimates which were screened out by the following procedure: situations with an obviously poor wind direction were excluded; in case of less obvious problems the calculation was repeated with a conditional sampling disregarding periods during which the 10% or 90%

fractile of an instantaneous profile was outside the measuring array. If the use of conditional sampling altered the c_{max} and σ_y estimates by more than 3% the results were rejected from Table 4. This is taken as an upper limit of the above-mentioned error caused by occasionally significant concentrations at the edges of the measuring array.

On account of the advection time the exposure of the sensors was delayed relative to the gas emission. The sample periods are therefore individual for each sensor array. Usually these periods T_{obs} are longer than the release duration T_{dur}, because the cloud is stretched in the wind direction. A close examination of Table 4 will reveal that the product $c_{max}\sigma_y$ is not always the same for the fixed- and moving-frame profiles. These disagreements have no mean bias, but a standard deviation of 7% and a maximum of 20%. This must be owing to curve fit errors, since the average data are based on identical time series. Indeed a visual inspection of all curve fits shows that the worst disagreement occurs when the fixed-frame profile is positively non-Gaussian. This supports our previous observation that the moving-frame profiles seemed to be more accurately determined by the Gaussian fits and probably more suitable for model comparison.

4.2. Vertical profiles

Britter [39] discusses vertical profiles of grounded heavy-gas plumes in the form $c = c_0\exp(-az^p)$. The shape of this profile is quite flexible and may vary from exponential ($p = 1$), to Gaussian ($p = 2$), and tophat ($p \to \infty$). Diffusion theory with power-law approximations to velocity and turbulent diffusivity profiles

$$u \propto z^m \text{ and } K_z \propto z^n \tag{9}$$

gives analytical results in accordance with the concentration profile mentioned and results in the relation $p = 2 + m - n$, see e.g. Sutton [40]. The exponent of the velocity profile is often set to $m = 1/7$, although this depends on atmospheric stability and the ratio between plume height and surface roughness. The eddy diffusivity in a neutral surface layer has linear height dependence $n = 1$, but Sutton [40] adjusts this to $n = 1 - m$ in order to produce a constant stress layer (i.e. a layer with constant momentum flux) and obtains $p = 9/7$. Britter and Snyder [41] measured concentration profiles in a wind tunnel and found that the shape parameter was $p \approx 1.5$ for plumes of neutral buoyancy but only $p \approx 1.0$ for dense gas plumes. At large distances downstream of the dense gas source the profile seemed to gradually develop into the profile observed for releases of neutral buoyancy $p \to 1.5$. The field measurements presented by Nielsen [28] showed that in the absence of source momentum the velocity distribution was insensitive to the stratification by the dense gas layer ($m \approx 1/7$), but the turbulent kinetic energy was more reduced inside the gas layer than above. This indicates a concave height dependence of the diffusivity profile $n > 1$ which might explain the smaller shape parameter p for the typical dense gas concentration profile.

Fig. 5 shows vertical profiles from trial 16 based on concentration measurements from gas sensors at 0.1, 0.75, 1.5, and 3 m height at 20 m distance, and at 0.1, 2, 4, and 9 m height at 70 and 238 m distance. Each sensor array had a centre-line mast which was sometimes hit directly and sometimes by the edge of the plume. The estimates of

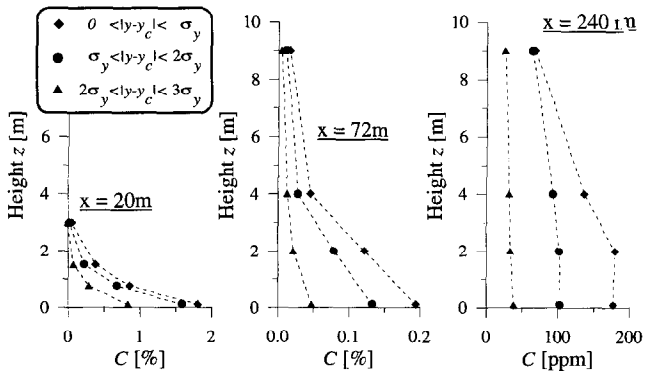

Fig. 5. Vertical average profiles in trial 16 using conditional sampling depending on the past position relative to the plume centre-line $y - y_c$.

the instantaneous plume centre-line y_c, based on measurements in the horizontal arrays, enable us to evaluate the vertical profile as a function of the distance from the instantaneous plume centre-line $y - y_c$. Because of the relatively short release durations the statistical uncertainty does, however, limit the spatial resolution of this moving-frame analysis. The values in Fig. 5 have been found using a conditional sampling which sorts the observations into just three bins depending on the instantaneous centre-line $y - y_c$. The advantage of this coarse distribution is that each profile in Fig. 5 represents at least three minutes of observation. The shape of the profiles from the first two distances is insensitive to the lateral position whereas the profiles from the last distance seem less regular.

In the light of the apparent profile similarity for variable plume positions in Fig. 5 (most obviously at the 20 and 70 m distances) we shall use all available measurements for determination of the vertical centre of mass $\bar{z}$ independent of the instantaneous plume position y_c. Curve fits to the generic concentration profiles described above by least squares error methods produced more than a decade of spreading in the shape parameter p, i.e. the observed profiles are too irregular for estimates of the profile shapes. Even two-parameter curve fits of fixed shapes, e.g. $p = 1$, resulted in great variation, and instead the plume centre of mass was estimated by stepwise linear interpolation

$$\bar{z}_{\text{est}} = \frac{\sum_{i=0}^{I-1} \int_{z_i}^{z_{i+1}} c(z)\, z\, \mathrm{d}z}{\sum_{i=0}^{I-1} \int_{z_i}^{z_{i+1}} c(z)\, \mathrm{d}z} \tag{10}$$

with linear extrapolation to the surface:

$$c_0 = \frac{z_2 c_1 - z_1 c_2}{z_2 - z_1} \tag{11}$$

Upward extrapolation of the concentration profile was considered to be too inaccurate, and the profiles were cut off at the highest sensor position. This implies that the plume depth is underestimated by Eq. (10). For a given shape parameter p we may however

correct the cut-off error. The concentration profile of Britter [39] may also be expressed by

$$c(z) = c_0 \exp\left[-\left(\frac{\Gamma(2/p)}{\Gamma(1/p)} \frac{z}{\bar{z}} \right)^p \right] \tag{12}$$

where we insert the gamma functions in order to scale the distribution with the centre of mass at $\bar{z}$. The estimated centre of mass $\bar{z}_{est}$ is expected to have the following relation with the cut-off height z_l, the shape parameter p and the true centre of mass $\bar{z}$:

$$\bar{z}_{est} \approx \frac{\int_0^{z_l/\bar{z}} \exp\left[-\left(\frac{\Gamma(2/p)\, z}{\Gamma(1/p)\, \bar{z}} \right)^p \right] \zeta \, d\zeta}{\int_0^{z_l/\bar{z}} \exp\left[-\left(\frac{\Gamma(2/p)\, z}{\Gamma(1/p)\, \bar{z}} \right)^p \right] d\zeta} \tag{13}$$

The cut-off height z_l is known, and this implies that the cut-off error $\Delta \bar{z}_{est} = \bar{z} - \bar{z}_{est}$ is a function of p which may be determined numerically. The two alternative values of $\Delta \bar{z}_{est}$ in Table 4 correspond to the profile shapes typical for dense gas dispersion ($p = 1$) and for a plume of neutral buoyancy ($p = 1.5$). It is a good approximation to estimate corrections for the shape parameter in the range $1 < p < 1.5$ by linear interpolation. The optimal profile fit will be further discussed in the next section.

In case of corrections larger than 15% the height estimates $\bar{z}_{est}$ were rejected from the table. This rules out all estimates from the 238 m distance, where the mast was simply too short for an accurate determination of the plume height.

5. Accuracy

The aim of this section is to evaluate the concentration measurements by a mass balance with the release rate and by comparison of data from adjacent concentration sensors.

5.1. Mass balance

The ground was wet after each trial and a few months later the grass in the exposed area seemed to be more vigorous than the surroundings indicating some fertilization caused by ammonia deposition. However according to the phase-transition model in the Appendix the amount of liquid-phase ammonia was insufficient for the deposition to have a significant effect on the plume mass balance. Therefore it seems to be a good check of the measured concentrations to compare the mass flux of the ammonia plume $\dot{m}_{pl}$ with the release rate $\dot{m}$, which is known to be within 5% of the measurements by the load cell under the release tank. The experimental design was optimized for determination of the plume dimensions, not the plume mass flux $\dot{m}_{pl}$, but we shall indirectly

estimate the mass flux by the average plume dimensions from Table 4. The mass flux is given by the integral

$$\dot{m}_{\mathrm{pl}} = \frac{M}{M_{\mathrm{air}}} \int\int \rho c u \, \mathrm{d}z \, \mathrm{d}y \tag{14}$$

where we approximate the mass ratio by cM/M_{air} since $c \ll 1$. This integral may be estimated in many ways. Here we neglect correlations in the turbulent signals and insert average density, concentration and velocity fields estimated by

$$c(y,z) = c_0 \exp\left[-\left(\frac{\Gamma(2/p)\, z}{\Gamma(1/p)\, \bar{z}} \right)^p - \frac{(y - y_c)^2}{2\sigma_y^2} \right] \tag{15}$$

$$\rho(c) = \frac{p_{\mathrm{air}} [(1-c) M_{\mathrm{air}} + c M_{\mathrm{eff}}]}{R T_{\mathrm{air}}} \tag{16}$$

$$u(c,z) = u_{10\,\mathrm{m}} \frac{\ln(z/z_0)}{\ln(10/z_0)} + \frac{cM}{(1-c) M_{\mathrm{air}} + cM} \frac{F_{\mathrm{jet}}}{\dot{m}} \tag{17}$$

The concentration field is modelled by the product of the vertical and horizontal profiles discussed in the previous section. The ground-level concentration c_0 is linked to the centre-line concentration $c_{\max}$ in Table 4 which was evaluated from the horizontal chain of measurements at height z_{r}.

$$c_0 = c_{\max}(z_{\mathrm{r}}) \exp\left[\left(\frac{\Gamma(2/p)\, z_{\mathrm{r}}}{\Gamma(1/p)\, \bar{z}} \right)^p \right] \tag{18}$$

For simplicity the mixture density ρ is calculated as if the release was an isothermal model gas with the "effective" molar weight M_{eff} estimated in Table 2. The velocity profile u is essentially logarithmic with a contribution from the jet flow force F_{jet}, i.e. a correction which considers the momentum as a conserved quantity and neglects the no-slip condition at the ground. These estimates are crude, but the magnitude of the density correction compared to $\rho = \rho_{\mathrm{air}}$ is just 1–3% at 20 m distance and essentially zero further downstream. The magnitude of the velocity correction is 15–30% at 20 m distance, 1–3% at 70 m distance, and negligible at 238 m distance.

The release parameters from Table 2 experiments are inserted together with the moving-frame plume dimensions from Table 4 and the mass flux integral is solved numerically. The average plume height is evaluated as $\bar{z} \approx \bar{z}_{\mathrm{est}} + \Delta \bar{z}_{\mathrm{est}}(p)$. In cases where the release duration was shorter than the period of gas observation, the estimated mass flux $\dot{m}_{\mathrm{pl}}$ is further corrected with the ratio $T_{\mathrm{dur}}/T_{\mathrm{obs}}$. Fig. 6 shows a comparison with the release rate $\dot{m}$ for vertical profiles of exponential shape ($p = 1$). The average mass balance is examined by regression lines through data from many trials and the correlation is found to be 1.02 for the sensor array at 20 m distance and 0.90 for the array at 70 m. This is in better agreement than the mass balance of the Desert Tortoise experiments [16], but it should be remembered that our procedure makes certain extrapolations and includes only cases where both $c_{\max}$, σ_y, and $\bar{z}$ are available from Table 4.

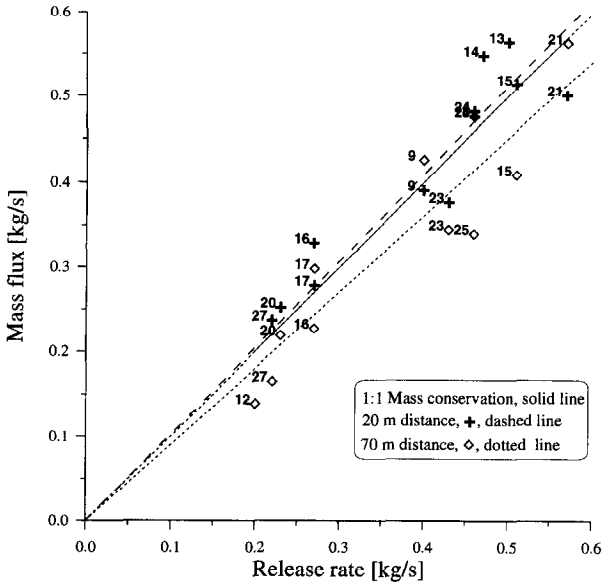

Fig. 6. Mass balance between field and source measurings assuming exponential shape of the vertical concentration profile.

The estimated mass flux is found to increase with the assumed shape parameter p. In this way the mass flux estimate may be tuned to a 1 : 1 correlation with the release rate if the profile shapes are described by $p = 0.97$ at 20 m distance and $p = 1.40$ at 70 m distance. These shapes are in good agreement with the review of Britter [39]. The mass estimated plume mass flux seems to be in reasonable agreement with the release rate and relatively insensitive to the unknown shape parameter p.

If the centre of gravity $\bar{z}$ had been estimated from curve fits, estimates would have been available also for the third sensor array, but the scatter in Fig. 6 would increase substantially. This was the reason for using simple linear interpolation when estimating the plume centre of gravity $\bar{z}_{est}$. With the daring assumptions of a vertical shape parameter of $p = 1.5$ at the 238 m distance, and assuming that the horizontal concentration profiles from Table 4 are correct, the mass balance may be used for rough estimates of the plume centre of gravity $\bar{z}$. These estimates are $\bar{z}_{est} = 13.5$, 9.2, 8.5, 13.7, 12.5, and 13.2 m for trials number 9, 15, 16, 23, 24 and 25 respectively.

5.2. Sensor intercomparison

Concentration sensors of different types were occasionally deployed in configurations which allow intercomparison of in situ measurements. The two measuring positions of each sensor pair had similar heights (± 0.05 m) and horizontal separations ~ 1 m, i.e. relatively close without compromising the measurements by flow distortion or other interference. Such sensor pairs were

- sonic anemometers with attached thermocouples and catalytic Dräger EX sensors distributed on the 0.75, 1.5 m level of the centre-line mast at 20 m distance

Table 5
Comparisons of signals from pairs of adjacent sensors of different types, showing mean and standard deviation ($\mu \pm \sigma$) of the ratio of average concentrations $\overline{c_1}/\overline{c_2}$ and cross correlations of filtered signals $R(c_1,c_2)$, see text for discussion

Signal types	Distance (m)	Pairs	Trials	$\overline{c_1}/\overline{c_2}$	$R(c_1,c_2)$
Sonic/Tc and Dräger EX	20	2	10	1.17 ± 0.23	0.71 ± 0.16
Uvic® and Dräger NH_3	238	3	1	0.90 ± 0.05	0.95 ± 0.15
Uvic® and Lidar	220	5	2	(1.44 ± 0.41)[a]	0.83 ± 0.04

[a]The ratios of ammonia and smoke concentration should be uniform, but not necessarily 1:1.

- Uvic® sensors and electrochemical Dräger NH_3 sensors at the 2, 4, and 9 m level of the centre-line mast at 238 m distance
- Uvic® sensors placed 2 m above terrain along the Lidar laser beam across the plume at 220 m distance

The different sensor types were calibrated independently and their intercomparison is a check of the measuring accuracy. Table 5 presents basic statistics of ratios of average concentration $\overline{c_1}/\overline{c_2}$ and cross correlation $R(c_1, c_2)$ of filtered signals. Time series from the fast-responding Uvic® sensors are preconditioned for the cross correlation analysis, using appropriate autoregressive filters to match the slow response of the Dräger sensors. Similarly the volume averaging of the Lidar has been simulated by a moving average filter on the Uvic® signal based on the estimated advection time through the Lidar averaging volume.

If two ideal sensors had been positioned at a single measuring point they would measure identical average concentrations (except for the Lidar which detects smoke not ammonia). In the light of the 10% relative accuracy required in section 2.4, the bias and scatter of the comparisons in Table 5 are not impressive. It should however be noted that these differences are partly caused by the different measuring volumes of the compared sensors and their spatial separation, e.g. a 1 m horizontal separation decreases the cross correlation coefficient of unfiltered signals to ~ 0.86, see below. Close examination of thermocouple time series indicates that these signals did not return sufficiently fast to the ambient temperature when the probe was outside the jet, and this explains the positive bias of the sonic/thermocouple estimates.

Conclusion: (1) the good overall accuracy suggested by the mass balance is not accompanied by equally successful intercomparisons of sensor pairs; (2) the sonic/thermocouple estimates have a positive bias; (3) the relatively successful intercalibrations for the far-end array provide the quality check missing in the mass balance analysis above.

6. Data analysis

The analysis carried out by participants of the main Fladis project is described in the joint final report edited by Duijm [6]. We shall make a brief introduction to this work and continue with complementary analyses made within the present project.

The University of Sheffield used the fast Uvic® measurements to validate a new model for the statistical distribution of concentration fluctuation time series, see Lewis and Chatwin [42]. Hamburg University made a wind-tunnel simulation of trial 16, and Electricité de France and Gaz de France made a comparison with the 3D k–ϵ MERCURE model, see Gabillard and Carissimo [43]. Both the wind-tunnel measurements and the numerical predictions were in excess of the field measurements. The comparisons were however based on fixed-frame statistics and it seems as if the moving-frame statistics from Table 4 are in better accordance with the model predictions, probably because the plume meandering was relatively weak in the wind-tunnel and not included in MERCURE. NSCR "Demokritos" compared the temperature–concentration relationship near the source to predictions by the 3D k–ϵ ADREA-HF model, see Andronopoulos et al. [44], and concluded that the model had difficulties with the degree of condensation in binary water–ammonia aerosols. The EU Joint Research Centre compared their 1D shallow layer type model with trial 16 data, see Würtz [45]. More references to these and previous works are listed by Duijm [6].

6.1. Concentration fluctuations

Fig. 7 shows a concentration time series measured by a fast-responding Uvic® sensor at the top of the centre-line mast at 237 m distance. The time series were digitized with 1000 Hz and reduced to 20 Hz time series by block averaging. Readings below a threshold level defined as three times the pretrial standard deviation are set to zero. This correction is very small because of the favourable signal-to-noise ratio. Comparatively long quiescent periods are observed when the plume moves away from the sensor. Rapid concentration fluctuations occur inside the plume as shown by the close-up frame in the lower part of the figure.

Fig. 8 shows power spectra of the concentration time series from Fig. 7 and simultaneous measurements by additional sensors at two lower levels of the mast. In

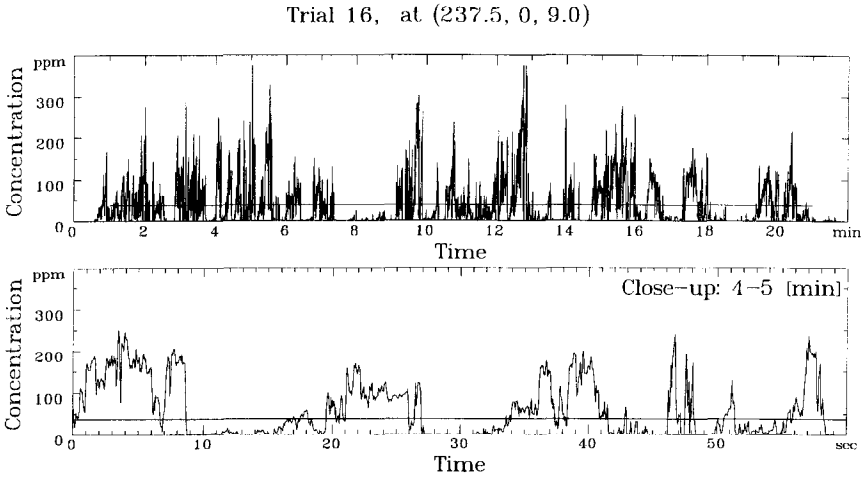

Fig. 7. Concentration measured by a fast-responding sensor and the 37.6 ppm average concentration.

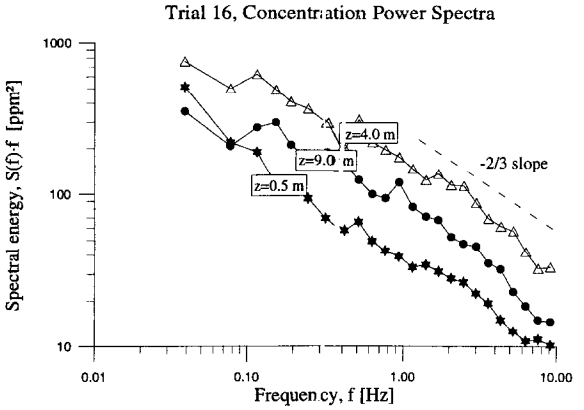

Fig. 8. Power spectra of concentration time series measured by fast-responding sensors at the centre-line mast at 240 m distance.

order to improve the statistical significance these series are divided into shorter ones with a length of 512 measuring points equal to ~25 s. The plotted spectra are calculated as averages of the 48 realizations and the estimated spectral energies are further averaged with a 20% relative band width. These are standard techniques for spectral analysis of atmospheric boundary layer turbulence, see Kaimal and Finnigan [46]. Low frequency estimates are excluded when the time series are divided into short realizations. A Fourier analysis without ensemble averaging would on the other hand produce inaccurate low frequency estimates not worth presenting owing to the short release duration. The high frequency part of the spectra are seen to follow the $S(f) \propto f^{-5/3}$ power law which is a characteristic of turbulence with an inertial subrange, see Pannofsky and Dutton [20]. No sign of instrumental smoothing is observed at the high frequencies.

The plot in Fig. 9 shows the cumulated probabilities $P\{C \leq c\}$ for each of the Uvic® signals used for the spectral analysis in Fig. 8. The curve added to each plot is a simple model which assumes a finite probability of zero concentration and a gamma distribution for the non-zero concentrations, i.e.

$$P\{C \leq c\} = P\{C = 0\} + P\{C > 0\}P\{C \leq c\,C > 0\}$$

$$= (1 - \gamma) + \gamma\left(1 - \frac{\Gamma\left(k, \frac{C}{\beta}\right)}{\Gamma(k)}\right) \tag{19}$$

where $\Gamma(k,C/\beta)$ and $\Gamma(k)$ are the incomplete and ordinary gamma functions, respectively, see Davis [47]. The plume intermittency γ is defined as the probability of non-zero concentration which is seen to decrease with the observation height. This statistical model has previously been used for concentration fluctuations in a convective mixed layer, see Deardorff [48], and it is of the model class defined by Chatwin and Sulivan [49]. Wilson [37] considers it a good approximation also for ground plumes

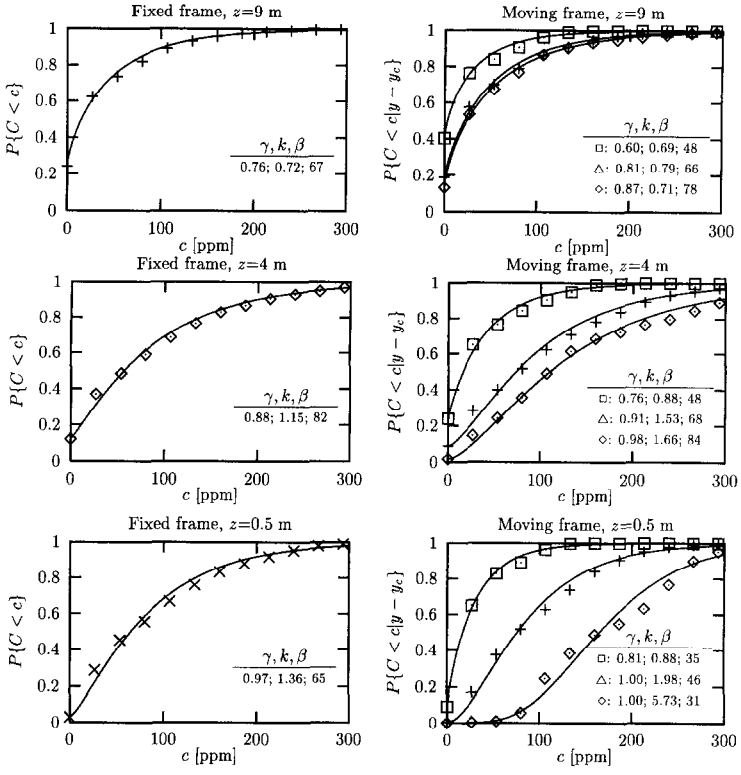

Fig. 9. Cumulated probability functions for concentrations in trial 16 measured by fast-response sensors at three heights at 240 m distance. The frames on the left-hand side show fixed-frame probabilities and the frames on the right-hand side show moving-frame probabilities marked ◇ for $y - y_c \leq \sigma_y$, △ for $\sigma_y < y - y_c \leq 2\sigma_y$, and □ for $2\sigma_y < y - y_c \leq 3\sigma_y$, depending on the distance between the mast and the plume centre-line.

although he recommends the almost equally simple log-normal distribution. The present model has not been tested against others, and it is preferred mainly because of its simple relation between the shape and scale parameters (k and β) and basic statistics

$$k = \frac{\mu^2}{\gamma\sigma^2 + (\gamma - 1)\mu^2} \tag{20}$$

$$\beta = \frac{\gamma\sigma^2 + (\gamma - 1)\mu^2}{\gamma\mu} \tag{21}$$

where μ and σ are the mean and standard deviation of the time series including zero concentration measurements. The curves added to Fig. 9 are calculated directly by the intermittency γ, mean μ and standard deviation σ, i.e. they are not curve fits. The distributions shown on the left-hand side of Fig. 9 are ordinary fixed-frame statistics. The average plume centre-line position was 22 m away from the mast, i.e. 0.88 times the fixed-frame plume spreading σ_y calculated in Table 4.

Yee [50] proposed a concentration fluctuation model based on a Gaussian distribution of the shifting plume centre-line and a gamma distribution for non-zero concentrations as above for concentrations in a moving frame of reference. The available time series are too short for high resolution estimates of such a moving-frame probability distributions and for statistical significance we just sort the observations into three classes, depending on the distance between the instantaneous plume centre-line position and the mast $y - y_c$. As for the vertical average profiles in Fig. 5, the instantaneous centre-line position y_c is deduced from simultaneous measurements by the horizontal chain of sensors. The derived moving-frame probability distributions are shown on the right-hand side of Fig. 9. The moving-frame intermittency γ appears to be variable in contrast to the assumption of Yee [50], but the shapes are reasonably well described by gamma functions. In the lower right frame, the shape of the distribution is seen to become steeper with increasing distance between mast and plume centre-line $y - y_c$. This is because the shape parameter k decreases with increasing signal intensity σ/μ. A similar change is seen by comparison of the near-centre-line moving-frame distributions (marked by $\diamond$) for the three different heights.

In trial 20 the fast concentration sensors were arranged for a study of the spatial structure of concentration fluctuations. The purpose was to study in-plume fluctuations caused by processes other than plume meandering. The instruments were aligned in the crosswind direction at 2 m height and 230 m distance and separated by irregular spacings. Fig. 10 shows the spatial correlation of two signals $c(y)$ and $c(y+\delta y)$ normalized by their standard deviation

$$R(y, y+\delta y) = \frac{\overline{c'(y)c'(y+\delta y)}}{\sigma(y)\sigma(y+\delta y)} \tag{22}$$

This correlation is evaluated for variable separation using signals from all combinations of sensors. The values for small separations are of main interest since the shape of the meandering plume may affect the correlations for large separations. The curve added to the figure is a best fit of the type $R = \exp[-(\delta y/b)^a]$ obtained by linear regression

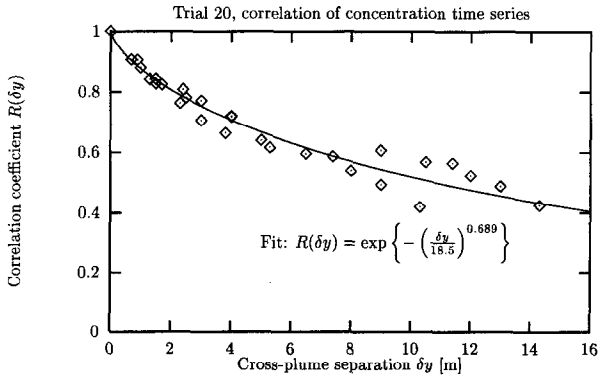

Fig. 10. Spatial correlation between concentration measurements by first sensors distributed perpendicular to the wind direction 230 m from the source at 2 m height.

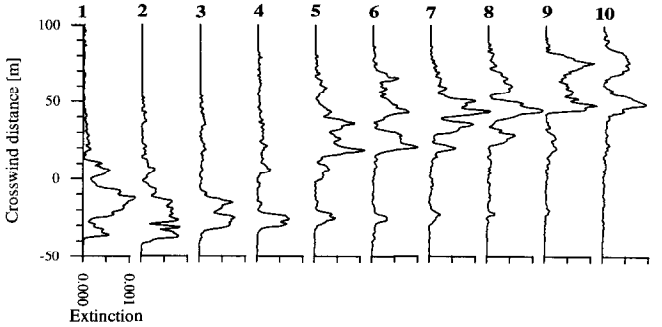

Fig. 11. Instantaneous crosswind Lidar profiles measured with intervals of three seconds in trial 25.

of transformed variables. The value of b probably relates to the plume dimension whereas the exponent a may be of a more fundamental interest. We note that the fitted value of a is close to $2/3$ as in the classic theory of the distance–neighbour function by Richardson [51], i.e. with a very fast decay for small separations which cannot be explained by plume meandering. It should be mentioned that periods with zero concentrations are included in the estimate and this tends to increase the correlation. The correlation function may therefore not be the perfect analysis of in-plume structure.

Fig. 11 shows ten instantaneous Lidar profiles measured with intervals of three seconds. This time increment corresponds to a plume advection of approximately 10 m. The shape of the profiles is far from Gaussian and sometimes it would be better to describe the plume as several parallel traces. A trace of gas is often located at the same distance for a long time, e.g. at a distance -30 m in profile number 3 to 8, but sometimes a trace suddenly appears on a new location, e.g. at a distance $+20$ m in profile number 5. Topological explanations for this behaviour are either that the plume lifts off at one distance and lands at another, or that the plume is broken into two pieces by a sudden change of the wind. The latter explanation seems most likely.

The sometimes abrupt changes of the Lidar profiles and point measurements by a fast sensor as in Fig. 7 indicate that plume meandering is not the only cause of concentration fluctuations.

6.2. Heat and temperature

The 8×8 thermocouples on the rig just in front of the source did not measure the detailed temperature field originally hoped for because of a thick layer of deposit. Instead fairly constant temperatures ~ 207 K were measured, i.e. much below the boiling point of 240 K. This piece of information is of practical interest when designing equipment for mitigation of accidental ammonia releases. The temperature of the aerosol from a flashing jet depends upon the vapour pressure of the gas. Liquid will continue to cool and evaporate while the vapour pressure is less than the saturation vapour pressure. The latter is continuously reduced by entrainment and as the latent heat of evaporation is large, the aerosol temperature can fall below the liquid boiling temperature. A simplistic model for the minimum temperature may be derived on the assumptions of (1)

homogeneous thermal equilibrium in the jet, (2) constant heat capacity c_p, and (3) mixing with dry air. Without a water component in the aerosols the minimum temperature will occur when the last ammonia droplet evaporates. The gas-phase molar ammonia concentration is the ratio between the ammonia saturation pressure and the total pressure $c = p_{sat}(T_{min})/p_{air}$. Concentration is also related to temperature by the enthalpy budget in Eq. (33). This leads to the relation

$$\frac{p_{sat}(T_{min})}{p_{air}} = \frac{(T_{min} - T_{air})\, M_{air} c_p^{air}}{\Delta H_0 + \left(M_{air} c_p^{air} - M c_p\right) T_{min} - T_{air}} \tag{23}$$

which is solved for the minimum temperature T_{min}. A typical combination of $T_{air} = 288$ K, $p_{air} = 1$ bar, and $\Delta H_0 = -20.5$ kJ mol^{-1} gives a minimum temperature of $T_{min} = 204$ K.

The top frame of Fig. 12 shows the temperature as a function of time and horizontal distance. The measurements were made by 23 thermocouples mounted with a 0.5 m separation on a string which was stretched across the cold jet at a height of 0.5 m. The distance was 10 m from the source, and this was just downwind of the point of jet touch-down. The jet was ~3 m wide and moved rapidly from side to side. Steady temperatures about 3°C lower than the ambient air were observed in a wider space around the jet. However this is probably a measuring error caused by evaporation of deposit from previous jet exposure. The frame below is a similar plot of measurements by 16 thermocouples mounted with a 0.11 m separation on a minimast on the ideal centre-line. The exposure of the minimast is in accordance with the horizontal positions of the plume shown by the upper frame.

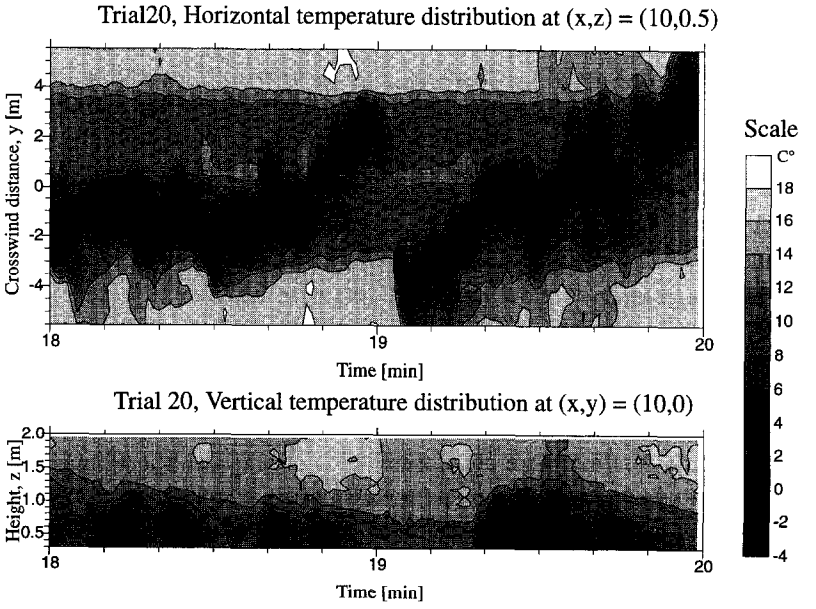

Fig. 12. Temperature 10 m from the source as a function of (1) time and crosswind distance, and (2) time and height above terrain. The contour levels are plotted for increments of 2°C.

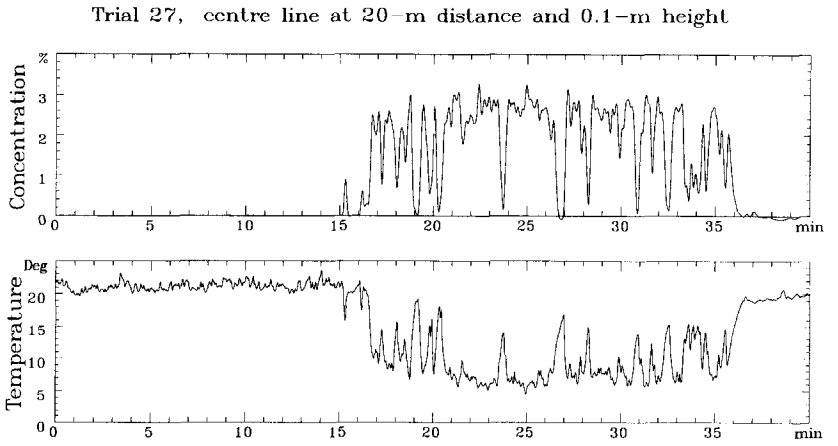

Fig. 13. Concentration and temperature from adjacent instruments.

Fig. 13 is a comparison of concentration and temperature measured at 20 m distance. In order to make the time series more comparable, the temperature signal has been averaged with a first-order auto-regressive filter with a time scale matching that of the concentration sensor. The correlation between the two signals is fair, but temperature fluctuations are present before the gas release. Also at this distance the thermocouple thermometer tends to measure too cold temperatures during short periods with low gas concentration, while the probe probably was wet and the surrounding gas phase undersaturated. In trial 27 the psychrometer on the reference mast had a wet-bulb temperature depression of $\sim 6°C$ (neglecting the ammonia content of the deposit), and this is close to the difference between the pretrial temperature and the maximum temperature during gas release as seen in Fig. 13. One might contemplate to revert the psychrometer equation and estimate the gas-phase temperature from the wet thermocouple temperature and the water vapour concentration known from the upstream measurement. These corrections would result in discrete temperature jumps whenever the surrounding gas phase is believed to change from the saturated to the undersaturated states. The correction would therefore be somewhat arbitrary and we cannot assume that a thermocouple covered by water droplets is in instantaneous thermal equilibrium. We shall therefore not attempt the correction, but note that sometimes the measured temperature is wrong and that the errors for this measurement position and this trial occur for low concentrations $c < 1.2\%$, see Fig. 13.

The main cause of the plume temperature deficit is the enthalpy deficit of the source. In case of perfectly adiabatic mixing the local plume temperatures must follow the enthalpy budget:

$$\overbrace{(T - T_{\text{air}}) \cdot [(1-c) \cdot M_{\text{air}} c_p^{\text{air}} + c \cdot M c_p] + \Delta H_{\text{con}}}^{\Delta H} = c \cdot \Delta H_0 \quad \text{(for wet adiabatic mixing)} \tag{24}$$

where ΔH_0 is the enthalpy difference between the released material at source and ambient conditions, and ΔH_{con} is the enthalpy of aerosol formation. This is further

explained in the Appendix, where it is applied together with a model for the density of a two-phase mixture of ammonia and humid air. In the following we use the field measurements to check the adiabatic mixing assumption, i.e. the postulated relation in Eq. (24). In order to determine the state of the aerosols we shall further assume that they are in homogeneous equilibrium with the gas phase, which, according to Kukkonen et al. [10], is reasonable for aerosol diameters less than 100 μm. The degree of condensation and the aerosol composition are deduced by the binary ammonia/water aerosol model of Wheatley [52]. The binary aerosol model includes the hygroscopic effect of ammonia and the heat of reaction when the ammonia dissociates in the water solution. However at 20 m distance the aerosols are almost pure water, and the reader may think of the heat of aerosol formation as

$$\Delta H_{\mathrm{con}} \approx -M_{\mathrm{H_2O}} L_{\mathrm{H_2O}} \left[(1-c) q_{\mathrm{air}} - q_{\mathrm{sat}}(T) \right] \tag{25}$$

where $M_{\mathrm{H_2O}}$ and $L_{\mathrm{H_2O}}$ are the molar weight and heat of evaporation for water, q_{air} is the water vapour concentration in the ambient air, and q_{sat} is the water vapour concentration corresponding to saturation. No aerosols are assumed to be present if $(1-c)q_{\mathrm{air}}$ is less than $q_{\mathrm{sat}}(T)$. The first step in the test of Eq. (24) ($\Delta H = c\Delta H_0$) is to evaluate the terms on the left-hand side, i.e. the enthalpy deficit in the field ΔH. In case of perfect adiabatic mixing the ratio between local enthalpy and concentration $\Delta H/c$ should be equal to the enthalpy deficit of the source ΔH_0. The temperature T is smoothed by an autoregressive filter matching the slow response of the concentration c. On a sunny day the ambient temperature T_{air} depends on the height above terrain, and the ambient temperature signal from the top of the mast is therefore corrected for the pretrial temperature difference $T - T_{\mathrm{air}}$. Only the trend of the ambient temperature T_{air} is of interest, so this signal is smoothed by a long averaging time.

Fig. 14 shows 20 s block averages of enthalpy deficit ΔH and concentration c based on the time series from Fig. 13 and simultaneous measurements from another sensor pair above. The block averages follow the linear regression lines with the exception of relatively large enthalpy deficits for low concentration situations at the 0.1 m level. These points are infected by the suspected thermocouple error discussed above, but the data were difficult to screen out by an objective criterion. Instead we just note that deviation was expectable for concentrations less than 1.2% at the 0.1 m level, and that block averaging may also distort the enthalpy for slightly higher average concentrations. The overall enthalpy to concentration ratio for the two heights is estimated by the slope of regression lines which has been forced through zero. The solid line corresponds to perfect adiabatic mixing of the released material. The overall enthalpy to concentration ratio for the sensor pair at the 0.1 m level has a deviation which is 1.9 times its uncertainty. This indicates additional heat input disregarded by the adiabatic mixing assumption in Eq. (24). The correlation of -16.4 kJ mol^{-1} NH_3 observed at the 0.1 m level corresponds to an "effective" molar weight $M_{\mathrm{eff}} = 73$ g mol^{-1}, which is 15% lower than the value calculated from the source measurements. With $M_{\mathrm{eff}} = 73$ g mol^{-1} the relative density deficit $\Delta\rho/\rho_{\mathrm{air}} \propto \Delta M_{\mathrm{eff}}/M_{\mathrm{air}}$ is 22% less than it would have been in the case of adiabatic mixing. The measurements of the sensor pair at the 1.5 m level do not deviate significantly from adiabatic mixing, probably because this mixture has not been in close contact with the ground. There is a theoretical possibility that the ammonia

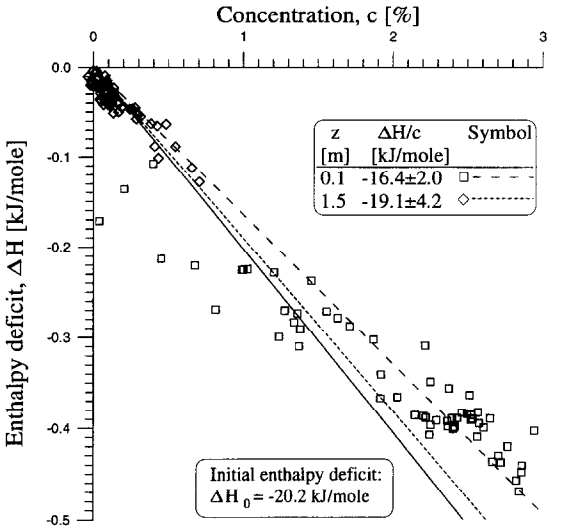

Fig. 14. Correlation of 20 s average enthalpy deficit and concentration. The dashed lines are obtained by linear regression through data from two heights 20 m downstream of the source. The solid line is the limit of wet adiabatic mixing according to Eq. (24).

plume could become lighter than air with sufficient heat supply, and according to Eq. (6) this buoyant plume limit corresponds to $\Delta H/c > -3.5$ kJ mol^{-1}. An enthalpy change of this magnitude seems most unlikely also downstream of the measuring point, where the plume temperature deficit and ground heat flux are modest.

6.3. Aerosol composition

In order to measure the composition of the liquid aerosols we took samples of the deposit in the release area. The aerosol collectors in trials 15 to 17 were placed along the ideal plume centre-line at heights following the path of the jet from 4 to 12 m distance. The amount of the collected material varied significantly with the distance to the source. Close to the source the collectors contained about 20 g, but at 10 and 12 m they contained only about 1 g, and therefore the uncertainty of the chemical analysis increases with downwind distance. Fig. 15 shows the composition of the sampled material as a function of distance from the source. The aerosol content is seen to change within a few meters from almost pure ammonia to almost pure water. The jet swept from side to side, i.e. not hitting the collectors all the time, and it took O(1) min to collect all samples after the release. It is possible that ammonia evaporated or that water condensed from the atmosphere during periods when the collector was exposed to the ambient air. Thus the concentration in each sample is a lower bound for the actual aerosol concentration. In trials 16 and 17 additional pieces of the ice deposit were taken directly from a rig placed 4 m from the source. The ammonia concentration of the ice was almost as high as in the aluminum envelope at this distance indicating that the deposit might have been an ammonia hydrate. Some of the measured concentrations are still

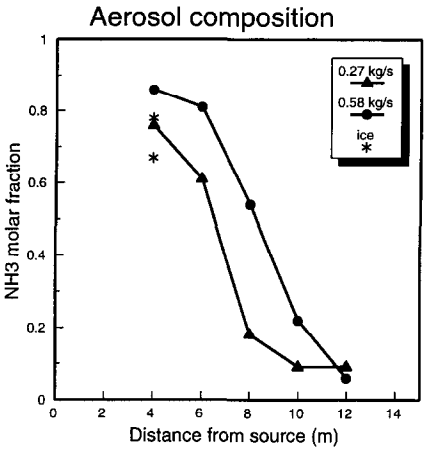

Fig. 15. Measured composition of liquid samples in trials 15 and 16 as a function of the distance from the source. The two ice samples are taken from trials 16 and 17, both with release rates of $\dot{m} = 0.27$ kg s^{-1}.

quite high which indicates that there was no serious ammonia evaporation from the samples.

7. Conclusions

The data set is unique because it enables validation of dense gas dispersion models with built-in transition to passive dispersion. A total number of 27 releases were made and a data set covering the best 16 releases has been prepared for distribution to all interested parties. The sensor layout provided estimates of plume dimensions at three distances.

The release rates and concentration measurements are validated. Release rates deduced from measurements in the release nozzle have been compared with independent measurements of the total ammonia spill and were found to agree within 5%. Estimates of the mass flux through the first two measuring arrays were within 10% of the validated release rate. This mass balance may even be tuned to a perfect correlation for both distances, if the heavy-gas effect on the vertical gas distribution observed by Britter and Snyder [41] is taken into account. The overall measuring accuracies confirmed by the mass balance, since the loss by ammonia deposition to the ground is expected to have been insignificant. In situ measurements from pairs of concentration sensors of different type and independent calibration show good correlation coefficients, although the average values used for comparison showed discrepancies that suggest some individual calibration problems. The overall accuracy is however adequate for the evaluation of heavy-gas dispersion models with transition to passive dispersion.

The data set includes detailed measurements of the wind field, turbulence and other meteorological parameters for an adequate input to numerical model comparison. Buildings upwind of the site affected the turbulence field but not the average wind field.

Models with built-in equilibrium boundary layer relations between flow and turbulent fluxes should be used with care.

Some of the participants in the main Fladis project made numerical models of one of the trials as well as a wind-tunnel simulations. In both simulations the plume was too wide with too low centre-line concentrations compared to fixed-frame statistics of the field measurements. The moving-frame statistics proposed in this article are in better accordance with the predictions of our partners, probably because the effect of plume meandering is excluded from the models. We suggest that the moving-frame statistics are more relevant for risk assessment of hazardous gas releases, perhaps used in combination with a probability for the variable plume centre-line. There is a need for heavy-gas models that take into account the variability owing to plume meandering.

Source measurements of exit pressure and temperature allow estimates of release enthalpy and jet flow force needed for model comparison. Specific plume enthalpy near the ground at 20 m distance was in excess of adiabatic mixing of air and ammonia consistent with the source measurements. This shows the existence of a heat input from the ground as previously observed in the laboratory experiments of Meroney and Neff [13] and Ruff et al. [14]. The observed enthalpy change corresponds to a 20% reduction of the plume buoyancy $\Delta\rho$. No sign of plume lift-off was observed.

The Fladis experiments applied longer release durations than was the case in other dense gas field experiments (up to 40 min) in order to obtain a better statistical accuracy. The combination of a few fast concentration sensors and slow concentration sensors detecting the variable plume centre-line provided concentration fluctuation statistics in both a fixed and a moving frame of reference. These were reasonable well described by a finite probability of zero concentration and a gamma distribution for non-zero concentrations. This is in accordance with the moving-frame probability model by Yee [50]. The moving-frame probability of zero concentration did, however, depend on the measuring position relative to the plume centre-line.

A remote-sensing Lidar was applied, and this is a novel technique in the context of heavy-gas experiments. The Lidar measurements demonstrated that the shape of instantaneous horizontal profiles is highly variable. Plume meandering caused by shifting wind directions is not the only cause of concentration fluctuations; small-scale turbulence causes in-plume fluctuations as well. The contaminant mass flow through a cross section of the plume is not necessarily steady as assumed in most dispersion models, and large-scale turbulent eddies may break the trace of the plume. Cross correlations of point measurements by fast concentration sensors seemed to have the $2/3$ dependence on the spatial separation predicted by the classic concentration fluctuation theory of Richardson [51].

The aerosol composition in the jet region was observed to change within a few meters in the downstream direction. This rapid change from almost pure ammonia to almost pure water suggests that the aerosols in the jet were close to homogeneous equilibrium in accordance with the model predictions of Kukkonen et al. [10]. The homogeneous equilibrium assumption is a computational advantage for the incorporation of phase transitions in heavy-gas dispersion models. Instantaneous equilibrium infers that aerosol dynamics and chemical reactions may be described by exchangeable submodels for different compounds as in DRIFT [4]. The deposit in the near-source region appeared to

be solid ice. This observation could either be in conflict with the current liquid aerosol theories (Wheatley [52] and Kukkonen et al. [10]) or imply that the ice is formed by the impaction of under-cooled liquid aerosols.

Finally we summarize current and future heavy-gas field experiments. The ongoing experiments of INERIS (France, winter 1996/1997) study liquid rain-out by impaction of two-phase jets on near-source obstacles. The recent experiments in Nevada [34] studied the effects of short transient releases, stable atmospheric conditions and an enhanced roughness typical of an industrial site. These French and American field activities focus on four outstanding problems in the understanding of heavy-gas dispersion. The effects of nearby obstacles seem to be a particularly difficult topic. The possible geometric configurations are endless and the flow field and dispersions around buildings are known to be complex even for gases of neutral buoyancy, see the review by Hosker [53]. An additional topic, so far not examined in large-scale field experiments, is heavy-gas dispersion on slopes or other terrain topographies.

8. List of notation

A	Nozzle area (m^2)
c	Concentration (mol mol^{-1})
C	Stochastic concentration (mol mol^{-1})
c_0	Concentration extrapolated to the ground (mol mol^{-1})
c_{max}	Plume centre-line concentration (mol mol^{-1})
c_{liq}	Liquid heat capacity (kJ kg^{-1} K^{-1})
c_p	Gas heat capacity (kJ kg^{-1} K^{-1})
c_p^{air}	Air heat capacity (kJ kg^{-1} K^{-1})
c_v	Heat capacity at constant volume (kJ kg^{-1} K^{-1})
f	Frequency (Hz)
F_{jet}	Jet flow force (N)
$I_\downarrow$	Insolation (W m^{-2})
k	Shape parameter of gamma distribution
K_z	Vertical diffusivity (m^2 s^{-1})
L	Monin–Obukhov length (m)
L_{H_2O}	Latent heat of water vaporization (kJ kg^{-1})
m	Power of wind profile
$\dot{m}$	Release rate (kg s^{-1})
$\dot{m}_{pl}$	Mass flux in plume (kg s^{-1})
M	Gas molar weight (kg mol^{-1})
M_{air}	Air molar weight (kg mol^{-1})
M_{H_2O}	Water molar weight (kg mol^{-1})
M_{eff}	"Effective" molar weight (kg mol^{-1})
n	Power of diffusivity profile
p	Shape parameter of vertical concentration profile
p_0	Exit pressure (bar)
p_{air}	Atmospheric pressure (mbar)

$p_{sat}(T)$	Gas saturation pressure (mbar)
$P\{\theta\}$	Probability of an event θ
$P\{\theta \Lambda\}$	Probability of an event θ under condition Λ
q	Concentration of water vapour (mol mol^{-1})
$q_{sat}(T)$	Water concentration at saturation (mol mol^{-1})
R.H.	Relative humidity (%)
R	Universal gas constant, $R = 8.314$ (J K^{-1} mol^{-1}))
$R(x,y)$	Statistical correlation of signal x and y
$S(f)$	Density of power spectrum ((%)^2 s)
T_{air}	Air temperature (K)
T_{boil}	Boiling point temperature (K)
T_{dur}	Release duration (min)
T_{obs}	Observation period (min)
T_0	Nozzle temperature (K)
u	Wind speed (m s^{-1})
u_*	Friction velocity (m s^{-1})
u_{10}	Average wind speed at 10 m (m s^{-1})
$\dot{V}$	Volumetric release rate (m^3 s^{-1})
x	Horizontal distance along ideal centre-line (m)
x_r	Downwind reference position (m)
X	Liquid phase contaminant concentration (mol mol^{-1})
χ	Gas-phase concentration (mol mol^{-1})
y	Horizontal distance in the lateral direction (m)
y_c	Crosswind position of plume centre-line (m)
z	Height above terrain (m)
z_r	Vertical reference height (m)
$\bar{z}$	Height of centre of gravity (m)
$\bar{z}_{est}, \Delta\bar{z}_{est}$	Estimate and correction for $\bar{z}$ (m)
z_0	Surface roughness (m)
α	Liquid fraction (mol mol^{-1})
α_{H_2O}	Degree of water condensation (mol mol^{-1})
β	Scale parameter of gamma distribution
Δ_{Dir}	Wind direction relative to ideal (deg)
$\Delta\rho$	Cloud density difference, $\Delta\rho = \rho - \rho_{air}$ (kg m^{-3})
ΔM	Molar weight difference, $\Delta M = M - M_{air}$ (kg mol^{-1})
ΔH	Specific enthalpy difference, $\Delta H = H(p,T) - H(p_{air},T_{air})$ (kJ mol^{-1})
ΔH_{con}	Heat of aerosol formation (kJ mol^{-1})
ΔH_{mix}	Heat of reaction in liquid phase (kJ mol^{-1})
ΔH_0	Enthalpy deficit of the source, $\Delta H = H(p_0,T_0) - H(p_{air},T_{air})$ (kJ mol^{-1})
γ	Concentration intermittency, $\gamma = P\{C > 0\}$
$\Gamma(s)$	Euler gamma function, $\Gamma(s) = \int_0^\infty t^{s-1}e^{-t}\,dt$
$\Gamma(s,a)$	Incomplete gamma function, $\Gamma(s,a) = \int_a^\infty t^{s-1}e^{-t}\,dt$

κ	von Karman constant = 0.4
μ	Average value
ψ_m	Diabatic correction to wind profile
ρ	Mixture density (kg m^{-3})
ρ_{air}	Density of ambient air (kg m^{-3})
ρ_{air}	Gas-phase density (kg m^{-3})
ρ_{liq}	Liquid phase density (kg m^{-3})
σ	Standard deviation
σ_{Dir}	Standard deviation of wind direction (deg)
σ_u	Standard deviation of wind speed (m s^{-1})
σ_y	Plume spreading (m)
$\angle$	Jet direction, vertical ↑ or horizontal →
Ø	Nozzle diameter (mm)

Acknowledgements

The Fladis field experiment was funded by the CEC ENVIRONMENT programme contract no. EV5V-CT92-0069, in collaboration with NUTEK who funded the Swedish project partners by contract no. D5226-92-11821. Additional funding was provided by the Swedish Rescue Board. We would like to acknowledge the work of our colleagues Mike Courtney, Ole Frost, Bent Mogensen, John Holm, Arent Hansen, Morten Frederiksen,Valter Thøfner, Søren Lund, Jan Nielsen, Sten Björk, Bengt Arne Tegner, Bo Juhl Andersen, Benny Kyngsman, Melker Nordstrand, Bill Evans, S.C. Cheah, and Tim Higgs. Our partners at Cambridge Environmental Research Establishment, H.A. Edmunds and Rex Britter, operated the ADMS model. Throughout the project we have been inspired by discussions with participants of the main Fladis project (Contract no. STEP-CT91-0125), i.e. our colleagues at the research institutes of TNO (NL), AEA Technology (UK), Building Research Establishment (UK), Health and Safety Executive (UK), Electricité de France, Gaz de France, Demokritos (Gr), Societé Bertin (F), European Joint Research Centre (I), and the Finnish Meteorological Institute, in collaboration with the Universities of Hamburg (D), Sheffield (UK), Cambridge (UK), Thessaloniki (Gr), and École Centrale de Lyon (F).

Appendix A. Approximate density of liquefied gas releases

During the main Fladis project it was discussed how to model a flashing jet with isothermal model gas in wind tunnels not prepared for toxic ammonia releases. This Appendix suggests the use of an effective molar weight which approaches the density for dilute mixtures after aerosol evaporation under a tentative assumption of adiabatic mixing. The simple model is compared to more accurate two-phase density calculations using release parameters of the field experiments.

Isothermal gas release. The density of an ideal mixture of air and gas is

$$\rho = \frac{p_{air}\left[Mc + M_{air}(1-c)\right]}{RT} \tag{A.1}$$

With an isothermal gas release the cloud temperature T and pressure p_{air} will be close to the ambient conditions, and the relative density difference simplifies to

$$\frac{\Delta\rho}{\rho_{air}} = \frac{\Delta M}{M_{air}} c \text{ (isothermal gas)} \tag{A.2}$$

where c is the molar gas concentration and ΔM is the molar weight difference between contaminant and air $M - M_{air}$.

Two-phase release in humid air. The density of a mixture of gas, humid air and liquid aerosols is found by addition of the specific volumes of the gas and liquid phase

$$\frac{1}{\rho} = \frac{1-\alpha}{\rho_{gas}} + \frac{\alpha}{\rho_{liq}} \tag{A.3}$$

where α is the molar liquid fraction. This may be quantified by the budget

$$\alpha = \alpha_{gas} c + \alpha_{H_2O} q(1-c) \tag{A.4}$$

where α_{gas} and α_{H_2O} are degrees of condensation for contaminant and water, and q is the water vapour concentration of the entrained air. With this notation the vapour concentrations become

$$\chi_{gas} = \frac{1-\alpha_{gas}}{1-\alpha} c \text{ and } \chi_{H_2O} = \frac{1-\alpha_{H_2O}}{1-\alpha} q(1-c) \tag{A.5}$$

These concentrations determine the average molar weight of the gas phase which has the following density:

$$\rho_{gas} = \frac{p\left[\chi_{gas} M + \chi_{H_2O} M_{H_2O} + (1 - \chi_{gas} - \chi_{H_2O}) M_{air}\right]}{RT} \tag{A.6}$$

When a compound is present in two phases, the partial vapour pressure must be equal to the saturation pressure. The vapour concentrations are therefore limited by

$$\chi \le \frac{p_{sat}(T)}{p_{air}} \tag{A.7}$$

where the vapour concentration is less than the limit of condensation only in the absence of liquid aerosols. For pure aerosols, e.g. in the case of immiscible liquids, the saturation vapour pressure curves P_{sat} will be functions of temperature only. Vapour pressures over binary aerosols are discussed below.

The mixture temperature T is determined by an enthalpy budget. Possible heat transfer from the ground or deposition of liquid aerosols are closely linked to the dispersion process, and in order to proceed we neglect these effects. Assuming adiabatic mixing the enthalpy budget is

$$\frac{\Delta H}{(T - T_{air})\left[(1-c) M_{air} c_p^{air} + c M c_p\right] + \Delta H_{con}} = c \Delta H_0 \text{ (adiabatic mixing)} \tag{A.8}$$

where c_p and c_p^{air} are the heat capacities of contaminant and ambient air. The left-hand side of this equation is the mixture enthalpy deficit relative to ambient temperature. The entrained air does not contribute to this, but the released material contributes with ΔH_0 defined as the enthalpy difference between the contaminant at source and ambient conditions. When the material evaporates from liquid phase, this enthalpy change is negative. The ratio of jet flow force and release rate $F_{jet}/\dot{m}$ may be taken as a typical velocity just after flash evaporation and this never exceeded 70 m s^{-1} in the Fladis experiments. This maximum velocity corresponds to a kinetic energy of 2.5 kJ kg^{-1} which is insignificant compared to the 1270 kJ kg^{-1} heat of ammonia evaporation, and therefore we neglect kinetic energy in the enthalpy budget in Eq. (A.8). The term ΔH_{con} is the heat of condensation which amounts to

$$\Delta H_{con} = \alpha_{gas} cML_{gas} + \alpha_{H_2O} q(1-c) M_{H_2O} L_{H_2O} + \alpha \Delta H_{mix} \tag{A.9}$$

where L_{gas} and L_{H_2O} are latent heats and ΔH_{mix} accounts for heat released after mixing in the liquid phase.

A binary phase-transition model. Wheatley [54] developed a model for the vapour pressures over a non-ideal two-component liquid phase. This was first calibrated for mixtures of water and hydrogen fluoride but later applied for water and ammonia [52]. The model describes the saturation vapour pressures of the mixture by

$$p_{gas}^{sat}(T,X) = p_{ref} X \exp\left(-\frac{A_{gas}}{T} + B_{gas}\right)$$

$$p_{H_2O}^{sat}(T,X) = p_{ref}(1-X)\exp\left(-\frac{A_{H_2O}}{T} + B_{H_2O}\right) \tag{A.10}$$

where X is the contaminant concentration in the liquid phase. The hygroscopic effect is modelled by variable A and B parameters which depend on liquid composition:

$$A_{gas} = A_{gas}^0 + (1 + r_a - r_a X)(1-X)^2 w_a$$

$$B_{gas} = B_{gas}^0 + (1 + r_b - r_b X)(1-X)^2 w_b$$

$$A_{H_2O} = A_{H_2O}^0 + \left(1 + \tfrac{3}{2} r_a - r_a X\right) X^2 w_a$$

$$B_{H_2O} = B_{H_2O}^0 + \left(1 + \tfrac{3}{2} r_b - r_b X\right) X^2 w_b \tag{A.11}$$

The w and r parameters are evaluated by fitting to experimental data. The vapour pressures automatically approach Raoult's law for ideal mixtures when the liquid composition is close to pure water ($X = 0$) or pure contaminant ($X = 1$). The enthalpy of mixing in the liquid phase is also related to the w and r parameters:

$$\Delta H_{mix} = -\left(1 + r_a - \tfrac{1}{2} r_a X\right) X(1-X) R w_a \tag{A.12}$$

The system of phase transitions in Eq. (A.10) must be solved by iteration of the liquid temperature and composition (X, T), or alternatively by the degrees of condensation (α_{H_2O}, α_{gas}) where the liquid composition is found from

$$X = \frac{\alpha_{gas}}{\alpha} c \tag{A.13}$$

Table 6
Parameters in Wheatley's binary phase-transition model for mixtures of ammonia and water; the w and r parameters are taken from Wheatley [52], and the A^0 and B^0 values are those used by Webber et al. [11]

$A^0_{NH_3} = 2747$ K	$w_a = -185$ K	$P_{ref} = 1$ N m^{-2}
$B^0_{NH_3} = 23.0$	$w_b = -0.34$	
$A^0_{H_2O} = 5314$ K	$r_a = -14$	
$B^0_{H_2O} = 25.9$	$r_a = -14$	

and the temperature T is found by the enthalpy budget in Eq. (A.8). Model parameters for ammonia are listed in Table 6.

Density after aerosol evaporation. The two-phase density calculation is complex compared to the simple formula for isothermal dispersion, but the solution after aerosol evaporation may be approximated by a very simple formula. At this stage $\Delta H_{con} = 0$, and the vapour concentrations are $\chi_{gas} = c$ and $\chi_{H_2O} = q(1-c)$. With these simplifications it is possible to derive the mixture temperature T from the enthalpy budget in Eq. (A.8) and to insert it in the relative density deficit of Eq. (A.3).

$$\frac{\Delta\rho}{\rho_{air}} = \frac{1 + c\dfrac{\Delta M}{M_{air}}}{1 + \dfrac{c\Delta H_0}{\left[(1-c)M_{air}c_p^{air} + cMc_p\right]T_{air}}} - 1 \text{ (dry adiabatic mixing)} \qquad \text{(A.14)}$$

In most cases the gas will be diluted already within a short distance from the source, and using $c \ll 1$ we linearize the expression to

$$\frac{\Delta\rho}{\rho_{air}} \approx c\left(\frac{\Delta M}{M_{air}} - \frac{\Delta H_0}{M_{air}c_p^{air}T_{air}}\right) \text{ (dry adiabatic mixing)} \qquad \text{(A.15)}$$

This linearized formula is very similar to that of Eq. (A.1), and the effect of enthalpy deficit is seen to be equivalent to excess molar weight. We therefore define an "effective" molar weight by

$$M_{eff} = M - \Delta H_0 / c_p^{air} T_{air} \qquad \text{(A.16)}$$

which may be used in wind tunnels for approximate modelling of two-phase releases. The formula is also a convenient approximation, e.g. when translating mass release rates to the volumetric release rates needed in the scaling laws for dense gas dispersion as defined by Britter and McQuaid [23] and König and Schatzmann [55].

Case studies. Fig. 16 illustrates the significance of aerosol formation in Fladis 9, Fladis 27 and Dessert Tortoise 4. The curves are based on Wheatley's hygroscopic ammonia model although the simpler immiscible-liquids model produced only slightly higher densities.

The plot on the left-hand side of Fig. 16 shows the relative density difference as a function of concentration, with addition of the M_{eff} approximation for Fladis 27 for comparison. Each curve falls into three parts: an almost linear path in the domain of dry mixing, a concave curve in the intermediate domain where the liquid phase consists

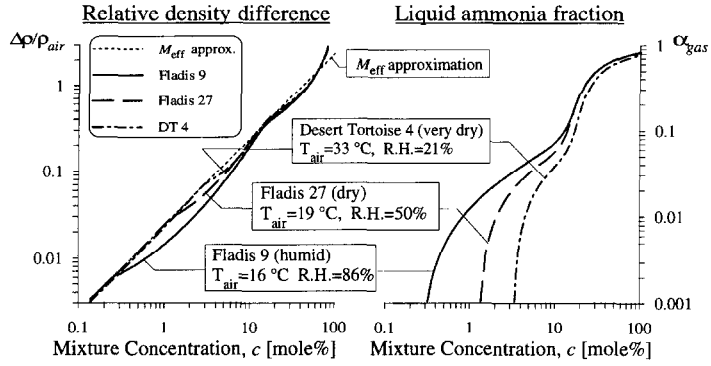

Fig. 16. Results of Wheatley's binary phase-transition model: (1) relative density difference as a function of concentration and comparison with the simplistic M_{eff} approximation, and (2) liquid ammonia fraction as a function of total ammonia concentration.

mainly of water, and another concave curve in the domain of almost pure ammonia aerosols. The different release enthalpies ΔH_0 slightly affect the curves in the domain of dry mixing. The main variation is however found in the intermediate domain which is influenced by variable air humidity. Further test cases show that the transition between dry and two-phase mixing is determined by the relative air humidity, whereas the magnitude of the deviation from the linear approximation is determined by the absolute air humidity q.

The M_{eff} approximation is sufficiently accurate in the domain of dry mixing. The question is to what extent the deviations for higher concentrations affect the dispersion process? There are two aspects to consider, the distance from the source to the limit of condensation and the magnitude of the error in the domain of liquid aerosols. In the present experiments the strong jet dominated the mixing in the domain of high concentrations, so the deviation of the simple approximation for concentrations higher than, say 10% NH_3, was unimportant. Furthermore we observed ice not liquid deposit in the near-source area so Wheatley's model could be unrealistic in this area. Our main concern is the deviations in the intermediate domain of almost pure water aerosols. In the Fladis experiments the typical concentration was 10% NH_3 where the jet first touched the ground about 10 m from the source and $\sim 2\%$ NH_3 in the first measuring array 20 m from the source. In the humid Fladis trial 9 the limit of condensation was 0.25% NH_3, i.e. almost as low as the typical concentration in the second measuring array, and the M_{eff} approximation predicted a $\Delta\rho$ difference which was up to 78% larger than in Wheatley's model. In the dry Fladis trial 27 the limit of condensation was $\sim 1.2\%$ NH_3 and the maximum relative error was $\sim 31\%$ near $\sim 3.9\%$ NH_3, i.e. the modification of the density effect owing to condensation was less significant in this trial.

Table 7 shows the limit of condensation and the maximum error of the M_{eff} approximation compared to Wheatley's model for $c < 10\%$ NH_3. The M_{eff} approximation should be avoided or used with care for high relative air humidities, which may be interpreted as Fladis trials 9, 12 and 20. Wind-tunnel modellers may consider to apply a

Table 7
The limit of condensation and the maximum error of the M_{eff} approximation for each of the Fladis trials

	6	7	9	12	13	14	15	16
Condensation (%NH_3)	0.62	0.85	0.25	0.48	1.05	1.05	0.86	0.80
Max. M_{eff} error (%)	33	22	78	59	29	32	40	40
	17	20	21	23	24	25	26	27
Condensation limit (%NH_3)	0.77	0.65	0.93	1.00	1.04	1.00	1.09	1.18
Max. M_{eff} error (%)	41	59	47	33	35	33	34	31

model gas with a lower molar weight than M_{eff} in order to reduce the near-source error, but this will be at the expense of too high densities further downstream.

The right-hand side of Fig. 16 shows the liquid ammonia fraction as a function of the total ammonia concentration. It is seen that ~ 90% of the ammonia was in the gas phase where the jet touched the ground increasing to ~ 98% in the first measuring array. It is therefore unlikely that a significant amount of the ammonia was lost by liquid deposition, and the gas-phase measurements at 20 m distance detected most of the total ammonia content.

References

[1] H.W.M. Witlox, Atmos. Environ. 28 (18) (1994) 2917.
[2] T.O. Spicer, J.A. Havens, in: S. Hartwig (Ed.), Heavy Gas and Risk Assessment—III, Battelle Institute, Frankfurt am Main, 1986, p. 73.
[3] D.L. Ermak, User's Manual for SLAB, UCRL-MA-105607, Lawrence Livermore National Laboratory, CA, 1990.
[4] D.M. Webber, S.J. Jones, G.A. Tickle, T. Wren, A Model of a Dispersion Dense Gas Cloud and the Computer Implementation DRIFT—II. Steady Continuous Releases, SRD-R587, AEA Technology, UK, 1992.
[5] D.M. Webber, J.S. Kukkonen, J. Hazard. Mater. 23 (1990) 167.
[6] N.J. Duijm, Research on the Dispersion of Two-phase Flashing Releases—Fladis, R94-451, TNO Institute of Environmental and Energy Technology, The Netherlands, 1994.
[7] M. Heinrich, R. Scherwinski, Propane Releases under Realistic Conditions—Determination of Gas Concentrations Considering Obstacles, TÜV 123UI00780, Technishe Überwachung Verein Norddeutschland, Germany, 1990.
[8] M. Nielsen, N.O. Jensen, Continuous Release Field Experiments with Obstacles, Risø-M-2923, Risø National Laboratory, Denmark, 1991.
[9] G.D. Kaiser, C. Walker, Atmos. Environ. 12 (1978) 2289.
[10] J. Kukkonen, M. Kulmala, J. Nikmo, T. Vesala, D. Webber, T. Wren, Atmos. Environ. 28 (1994) 2763.
[11] D.M. Webber, G.A. Tickle, T. Wren, J. Kukkonen, Mathematical Modelling of Two-phase Release Phenomena in Hazard Analysis, SRD-R584, AEA Technology, UK, 1992.
[12] I.G. Lines, A Review of the Manufacture, Uses, Incidents and Hazard Models for Hydrogene Flouride, HSE 79/1995, Health and Safety Executive, UK, 1995.
[13] R.N. Meroney, D.E. Neff, J. Heat Transfer 108 (1986) 9.
[14] M. Ruff, F. Zumsteg, T. Fannelp, J. Hazard. Mater. 19 (1988) 51.
[15] R.E. Britter, Assessment of the Use of Cold Gas in a Windtunnel to Investigate the Influence of Thermal Effects on the Dispersion of LNG Vapour Clouds, TR-14-1987, Cambridge University, Engineering Department, UK, 1987.

[16] H.C. Goldwire, T.G. McRae, G.W. Johnson, D.L. Hipple, R.P. Koopman, J.W. McClure, L.K. Morris, R.T. Cederwall, Desert Tortoise Series Data Report—1983 Pressurized Ammonia Spills, UCID-20562, Lawrence Livermore National Laboratory, CA, 1985.
[17] A. Resplandy, Chim. Ind. Gén. Chim. 103 (1969) 691 (in French).
[18] D.B. Pfenning, S.B. Millsap, D.W. Johnson, in: J. Woodward (Ed.), International Conference on Vapor Cloud Modeling, Boston, AIChE, 1987, pp. 81-115.
[19] H.A. Edmunds, R.E. Britter, The Effect of Nearby Buildings on a Passive Release, FM89/1, Cambridge Environmental Research Consultancy, 1994.
[20] H.A. Panofsky, J.A. Dutton, Atmospheric Turbulence, John Wiley and Sons, New York, 1984.
[21] S. Ott, GReAT Jet Model (Internal report), Risø National Laboratory, 1990.
[22] T. Vesala, J. Kukkonen, Atmos. Environ. 26A (9) (1992) 1573.
[23] R.E. Britter, J. McQuaid, Workbook on the Dispersion of Dense Gases, HSE 17/1988, Health and Safety Executive, UK, 1988.
[24] M. Nielsen, R. Bengtsson, C. Jones, K. Nyrén, S. Ott, D. Ride, Design of the Fladis Field Experiments with Dispersion of Liquefied Ammonia, Risø-R-755(EN), Risø National Laboratory, Denmark, 1994.
[25] M. Nielsen, N.O. Jensen, S. Ott, in: Ninth Symposium on Turbulence and Diffussion, Roskilde 1990, American Meteorological Society, 1990, p. 145
[26] M.J. Leck, D.J. Lowe, J. Hazard. Mater. 11 (1985) 65.
[27] K. Nyrén, D.J. Ride, C.D. Jones, Ice Baby—Measurings of Concentration Fluctuations in a Forest Area in Winter Conditions, FOA C40320-4.5, National Defence Research Establishment, Ume, Sweden, 1994.
[28] M. Nielsen, J. Loss Prev. Process Ind. 4 (1991) 29.
[29] H.E. Jørgensen, T. Mikkelsen, J. Streicher, H. Herrmann, C. Werner, E. Lyck, Appl. Phys. B 64 (1997) 355.
[30] S. Ott, Measurements of Temperature, Radiation and Heat Transfer in Natural Gas Flames, Risø-R-703(EN), Risø National Laboratory, Denmark, 1993.
[31] M. Nielsen, S. Ott, A Collection of Data from Dense Gas Experiments, Risø-R-845(EN), Risø National Laboratory, Denmark, 1995.
[32] C.A. Paulson, J. Appl. Meteorol. 9 (1970) 57.
[33] D. Golder, Boundary-Layer Met. 3 (1972) 47.
[34] S.R. Hanna, K.W. Steinberg, in: S.E. Gryning, F.A Schiermeier (Eds.), Air Pollution Modeling and its Application—XI, Plenum Press, New York, 1996, pp. 481-490.
[35] K. Nyrén, S. Winter, J. Hazard. Mater. 14 (1987) 365.
[36] S.R. Hanna, D.G. Strimaitis, J.C. Chang, in: International Conference and Workshop on Modeling and Mitigating the Consequences of Accidental Releases of Hazardous Materials, New Orleans, AIChE, 1991, pp. 345-368.
[37] D.J. Wilson, Concentration fluctuations and averaging time in vapor clouds, AIChE, 1995.
[38] M. Nielsen, Surface Concentrations in the Fladis Field Experiments, Risø-I-995(EN), Risø National Laboratory, Denmark, 1996.
[39] R.E. Britter, in: J.S. Puttock (Ed.), Stably Stratified Flow and Dense Gas Dispersion, Clarendon Press, UK, 1988, pp. 1-38.
[40] O.G. Sutton, Micrometeorology, McGraw-Hill, 1953.
[41] R.E. Britter, W.H. Snyder, J. Hazard. Mater. 18 (1988) 37.
[42] D.M. Lewis, P.C. Chatwin, Environmetrics 6 (1995) 583.
[43] M. Gabillard, B. Carrissimo, Project Fladis—Pressurized Flashing Releases—Part III. Ammonia Releases, M. CERMAP 941.640, Gaz de France, France, 1994.
[44] S. Andronopoulos, J.G. Bartzis, J. Würtz, D. Asimakopoulos, J. Hazard. Mater. 37 (1994) 327.
[45] J. Würtz, A Transient One-dimensional Shallow Layer Model for Dispersion of Denser-than-air Gases in Obstructed Terrain under Non-isothermal Conditions, EUR 15343 EN, Joint Research Centre, Commision of the European Communities, 1993.
[46] J.C. Kaimal, J.J. Finnigan, Atmospheric Boundary Layer Flows, Oxford University Press, 1994.
[47] P.J. Davis, in: M. Abramowitz, I.A. Stegun (Ed.), Handbook of Mathematical Functions, AMS 55, US National Bureau of Standards, 1964, pp. 253-294.
[48] J.W. Deardorff, G.E. Willis, in: A. Venkatram, J.C. Wyngaard (Eds.), Lectures on Air Polution Modeling, American Meteorological Society, 1988, pp. 357-384.

[49] P.C. Chatwin, P.J. Sullivan, J. Fluid Mech. 212 (1990) 533.
[50] E. Yee, R. Chan, P.R. Kosteniuk, G.M. Chandler, C.A. Biltoft, J.F. Bowers, Boundary-Layer Meteorol. 67 (1994) 11.
[51] L.F. Richardson, Proc. R. Soc. A 110 (1926) 709.
[52] C.J. Wheatley, Discharge of Liquid Ammonia to Moist Atmospheres, SRD/HSE-R410, UK Atomic Energy Authority, 1987.
[53] R.P. Hosker, Jr., in: D. Randerson (Ed.), Atmospheric Science and Power Production, DOE/TIC 27601, US Department of Energy, 1984, pp. 241-326.
[54] C.J. Wheatley, A Theory of Heteorogeneous Equilibrium between Vapour and Liquid Phases of Binary Systems and Formulae for the Partial Pressures of HF and H_2O Vapour, SRD-R357, UK Atomic Energy Authority, 1986.
[55] G. König-Langlo, M. Schatzmann, Atmos. Environ. 25A (1991) 1189.